Modeling of Geophysical Flows – Analysis of Models and Modeling Assumptions Using UQ

Ali Akhavan Safaei[1], Andrea Bevilacqua[2], Abani K. Patra[1,3], E. Bruce Pitman[4], and Marcus I. Bursik[2]

[1] *Dept. of Mech. and Aero. Eng., University at Buffalo, Buffalo NY 14260*
[2] *Dept. of Geology, University at Buffalo, Buffalo NY 14260*
[3] *Comp. Data Science and Eng., University at Buffalo, Buffalo NY 14260*
[4] *Dept. of Materials Design and Innovation, University at Buffalo, NY, 14260*

{abani,aliakhav,abevilac}@buffalo.edu

Abstract

Dense large scale granular avalanches are a complex class of flows with physics that has often been poorly captured by models that are computationally tractable. Sparsity of actual flow data (usually only a posteriori deposit information is available) and large uncertainty in the mechanisms of initiation and flow propagation make the modeling task challenging and a subject of much continuing interest. Models that appear to represent the physics well in certain flows turn out to be poorly behaved in others due to intrinsic mathematical or numerical issues. Nevertheless, given the large implications on life and property many models with different modeling assumptions have been proposed.

While, inverse problems can shed some light on parameter choices it is difficult to make firm judgements on the validity or appropriateness of any single or set of modeling assumptions for a particular target flow or potential flows that needs to be modeled for predictive use in hazard analysis. We will present here an uncertainty quantification based approach to carefully, analyze the effect of modeling assumptions on quantities of interest in simulations based on three established models (Mohr-Coulomb, Pouliquen-Forterre and Voellmy-Salm) and thereby derive a model (from a set of modeling assumptions) suitable for use in a particular context. We also illustrate that a simpler though more restrictive approach is to use a Bayesian modeling average approach based on the limited data to combine the outcomes of different models.

We juxtapose observation data to the simulation results, only with the purpose to maintain a link to the real occurrence of a geophysical flow representing a possible outcome of the case studies described. The fundamental focus of this paper is the exploration of the dynamics of the simulated flows, enabling a notion of the contribution of different mechanisms or models elements inside the simulation procedure, in a fully quantitative, predictive-use oriented and statistical framework.

1 Introduction - Andrea

1.1 Geophysical mass Flows - Andrea

Geophysical mass flows include debris and mud flows, landslides, snow and rock avalanches, glacier flows, pyroclastic surges, block and ash flows, and pumice flows, lahars, jokulhaups and many other examples. These flows are sometimes tens of kilometers in length and may travel at speeds as fast as hundreds of meters per second. Their deposits can be as much as tens of meters deep and kilometers long. In other words, there is no single universal description of a "typical" geophysical mass flow. Different types of flows are the results of different types of mechanisms/processes and hence different types of flows will have significantly different physical characteristics.

The rheology complexity of the fluidized material, the mathematical problem of modeling and computing, make the description of the dynamics of those flows really challenging. In many cases the flows are *shallow*, i.e. the horizontal dimension is significantly larger than the flow depth. This assumption allows a depth-integration of the governing 3D Navier-Stokes-type equations, leading to the formulation of the 2D Shallow Water Equations (SWE), also called Saint Venant Equations (Batchelor, 2000; Luca et al., 2016). A large number of studies were focused on the modeling of depth-averaged geophysical flows, many of them reviewed in Pudasaini and Hutter (2007). In Savage and Hutter (1989); Jaeger et al. (1989); Hutter et al. (1993); Fraccarollo and Toro (1995); Dade and Huppert (1998) a depth-averaged model for granular material was first developed, and applied to the case study of an inclined plane, following the Mohr-Coulomb rheology (MC).

The modeling of a granular flow down an inclined plane was explored in detail by several further studies, both theoretical and experimental (Pouliquen, 1999; Ruyer-Quil and Manneville, 2000; Silbert et al., 2001; Balmforth and Kerswell, 2005; Bursik et al., 2005; DaCruz et al., 2005; Lajeunesse et al., 2005). Terrain erosion effects were explored (Pitman et al., 2003a; Edwards and Gray, 2015), and also material deposition and self-channelling effects (Mangeney-Castelnau et al., 2005, 2007). The inclined plane experiments also led to the development of the Pouliquen-Forterre rheology (PF), assuming a changing frictional behavior as a function of flow regime, allowing for an improved wave-propagation and vortices-evolution in the flow (Pouliquen, 1999; Forterre and Pouliquen, 2002; Pouliquen and Forterre, 2002; Forterre and Pouliquen, 2003; Forterre, 2006; Jop et al., 2006).

In parallel to the earth avalanches experiments, the study of snow avalanches led to the development of the Voellmy rheology (VS) (Voellmy, 1955; Bartelt et al., 1999; Salm et al., 1990; Salm, 1993; Bartelt and McArdell, 2009). Such rheology assumes a velocity dependent *turbulent* friction term in addition to the Coulomb friction. Many experimental and theoretical studies were developed in this framework (Gruber and Bartelt, 2007; Kern et al., 2009; Christen et al., 2010; Fischer et al., 2012).

In Iverson (1997); Iverson and Denlinger (2001); Denlinger and Iverson (2001, 2004); Iverson et al. (2004) the depth-averaged model was further studied and applied on a realistic terrain. Wieland et al. (1999); Gray et al. (1999, 2003) tested the model on fast avalanches, exploring the effects of channelizing/chuting topographies. A compensation for the effect of earth pressure changes was implemented and explored in detail (Pirulli et al., 2007; Pirulli and Mangeney, 2008), as well as the effects of significant curvature in the terrain (Greve et al., 1994; Pudasaini and Hutter, 2003; Fischer et al., 2012). Several specific studies on the pore pressure effects on the flow initiation and fluidization were developed (Savage and Iverson, 2003; Iordanoff and Khonsari, 2004; Iverson and George, 2014). A two-phase model was also implemented to replicate heterogenous flows, with a significant quantity of interstitial fluid (Pitman and Le, 2005) All these complex modeling choices correspond to alternative or cumulative physical assumptions, and they are sometimes very difficult to ponder, compare or combine together.

A particular interest is associated with the specific efforts devoted to the modeling of volcanic mass flows with SWE (Freundt and Bursik, 1998; Bursik et al., 2005; Saucedo et al., 2005; Kelfoun and Druitt, 2005; Charbonnier and Gertisser, 2009; Kelfoun et al., 2009; Procter et al., 2010; Sulpizio et al., 2010; Kelfoun, 2011; Charbonnier et al., 2013). Volcanoes are a great source of a rich variety of geophysical flows examples, as well as field data.

In this study we will take advantage of the TITAN2D code solving the shallow-water equations, and implementing the MC, PF and VS rheologies in the same platform (Pitman et al., 2003b; Patra et al., 2005, 2006; Yu et al., 2009; Aghakhani et al., 2016). The TITAN2D code already achieved many successful applications in the simulation of different geophysical mass flows, with specific peculiarities (Sheridan et al., 2005; Rupp et al., 2006; Norini et al., 2009; Charbonnier and Gertisser, 2009; Procter et al., 2010;

Sheridan et al.; Sulpizio et al., 2010; Capra et al., 2011). Several studies involving TITAN2D were recently directed towards a statistical study of geophysical flows, focusing on the uncertainty quantification and propagation (Dalbey et al., 2008; Dalbey, 2009; Stefanescu et al., 2012b,a), or on the more efficient production of hazard maps (Bayarri et al., 2009; Spiller et al., 2014; Bayarri et al., 2015; Ogburn et al.). This study for the first time applies a statistical approach to the detailed exploration of the stresses and powers in the flow, as well as on the velocity and height and inundated area. The former have a strong link with the dynamical equation terms, the latter have a direct link to field observation and hazard assessments. Our purpose is the achievement of a quantitative and statistical understanding of the different physical assumptions, both inside the flow and on the outputs.

1.2 Overview of the case studies - Andrea

The first case study assumes very simple boundary conditions, and correspond to an experiment fully described in Webb (2004); Bursik et al. (2005); Webb and Bursik (2016). It is a classical flow down an inclined plane experiment, including a change in slope to an horizontal plane (Fig. 1).

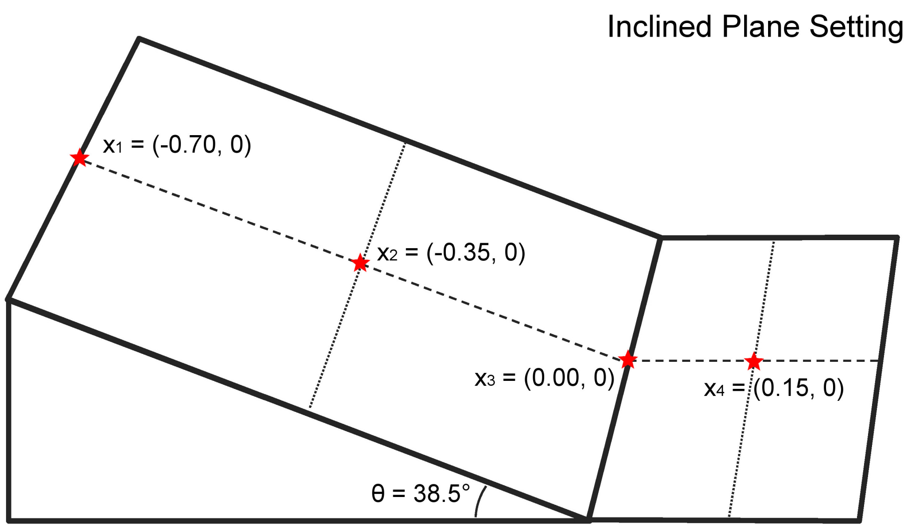

Figure 1: Inclined plane description, including local samples sites (red stars).

A second case study is a block and ash flow down the slope of Volcán de Colima (México) - an andesitic stratovolcano that rises to 3,860 m above sea level, situated in the western portion of the Trans-Mexican Volcanic Belt (Fig. 2). Historically, it has been the most active volcano in México (la Cruz-Reyna, 1993; Zobin et al., 2002; González et al., 2002). During July 10^{th}-11^{th} 2015, the volcano underwent its most intense eruptive phase since its Subplinian-Plinian 1913 AD eruption (Saucedo et al., 2010; Zobin et al., 2015; Reyes-Dvila et al., 2016; Capra et al., 2016). The modeling of pyroclastic flows generated by explosive eruptions and lava dome collapses of Volcán de Colima is a well studied problem (Martin Del Pozzo et al., 1995; Sheridan and Macas, 1995; Saucedo et al., 2002, 2004, 2005; Sarocchi et al., 2011; Capra et al., 2015). The volcano has been already used as a case study in several research involving the Titan2D code (Rupp, 2004; Rupp et al., 2006; Dalbey et al., 2008; Yu et al., 2009; Sulpizio et al., 2010; Capra et al., 2011; Aghakhani et al., 2016).

In this study the flow is assumed to be generated by the gravitational collapse of a paraboloid dome placed close to the summit area. A dome collapse occurs when there is a significant amount of recently-extruded highly-viscous lava piled up in an unstable configuration around a vent. Further extrusion and/or externals forces can cause the still hot dome of viscous lava to collapse, disintegrate, and avalanche downhill (Bursik et al., 2005). The hot, dense blocks in this “block and ash” flow will typically range from centimeters to a few meters in size. The matrix is composed of fine ash from the comminuted blocks. Computations were performed on a DEM with 5m-pixel resolution, obtained from LiDAR data acquired in 2005 (Davila et al., 2007; Sulpizio et al., 2010).

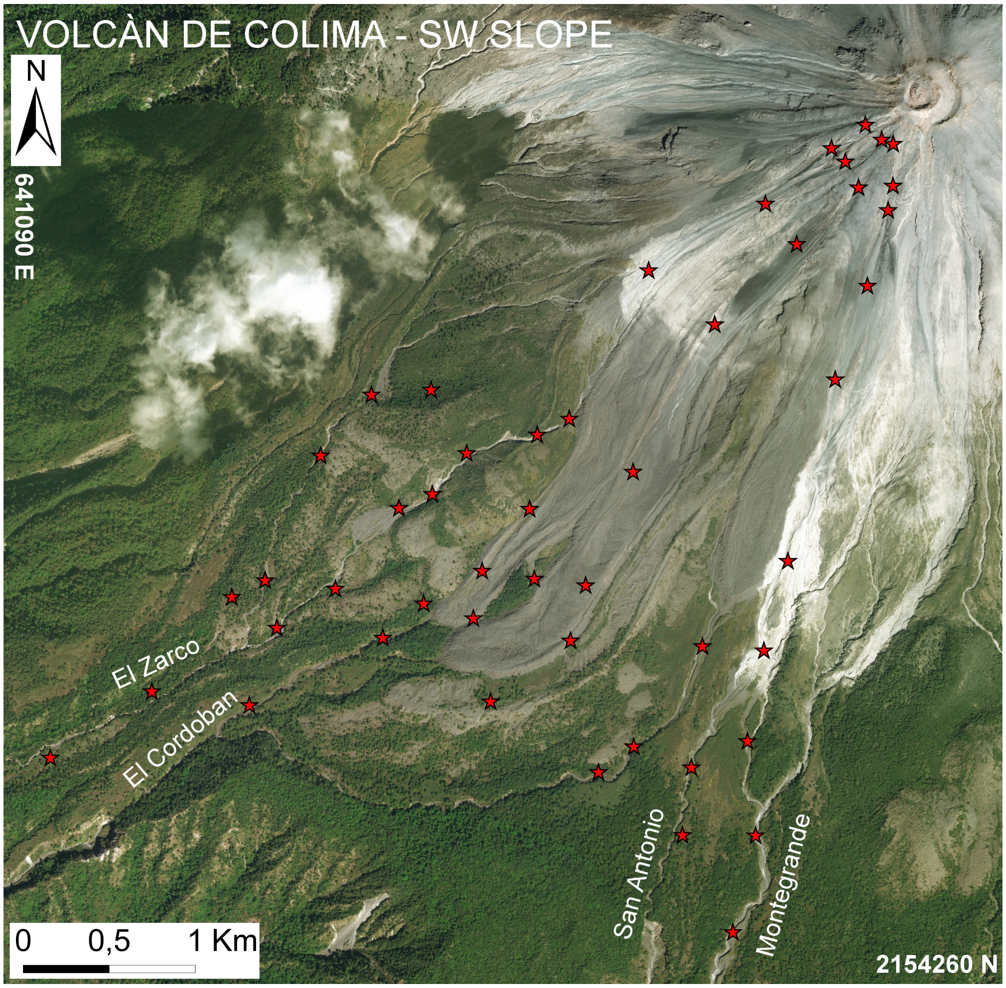

Figure 2: Volcán de Colima (México) overview, including local samples sites (red stars) and four major ravines channeling the flow. Reported coordinates are in UTM zone 13N.

2 Review of Models – Ali + Andrea

2.1 Modeling Assumptions - Ali + Andrea

Any numerical model of geophysical mass flows relies on several physical and mathematical assumptions. We will classify them in two groups - the general assumptions and the rheology assumptions. The main focus of this study is on the latter group, but in future the same procedure could be applied to the former.

1. The moving mass was assumed to be *volume preserving*. Since the dynamics define the motion, assuming volume preserving is an adequate approximation.
2. Geophysical mass flows are mostly assumed to be *free surface* flows consist of granular material (i.e. a large collection of discrete particles, frequently with interstitial fluid, and whatever else that get caught in the flow path). In general, the “typical particle” is small compared to the depth and length

of the flowing mass and makes it reasonable to model the flowing material as a continuum which implies that the thickness of sliding and deforming body extends over several particle diameters. Therefore, we can consider an "equivalent flowing material" whose rheological properties are chosen to approximate the bulk behavior that is expected of an actual mass flow; however, the properties of this "equivalent material" may not correspond to those of any component of the actual mass flow.

3. According to the *geometries* of geophysical mass flows, numerous models make the *shallowness* approximation for their numerical simulation. In this approximation, the flow depth is assumed to be at least an order of magnitude less than the characteristic length of the flowing material.
4. The shear stresses lateral to the main flow direction can be neglected.
5. The body of mass is supposed to be in *isothermal* state or, if not, thermal effects can be ignored.
6. The flowing mass is assumed to be consisted of an *incompressible* granular continuum material. This means that we are allowed to ignore variations of density due to the void ratio (density preserving assumption).
7. Motion of the bulk of mass consists of "shearing within the deforming mass" and "sliding along the basal surface". However, based on the observations, the shearing deformation commonly takes place within a very small boundary layer, so that it is justified to collapse this boundary layer to zero thickness and to combine the sliding and shearing velocity to a single sliding law with a somewhat larger modelled *sliding velocity*. This then effectively means that variations of the material velocities across the flow depth may be ignored and *depth-averaged* equations may be employed (Savage and Hutter, 1989; Hutter et al., 1993). Details on the integration of continuum models for shallow free surface flows can be studied in (Pudasaini and Hutter, 2007).
8. The shallowness assumption gives a *hydrostatic* expression for the normal pressure in the direction perpendicular to the basal surface. Moreover, the downslope and cross-slope pressure components are assumed to be varying linearly with the normal pressure component through the flow depth. The coefficient could either be defined based on the rheology model or be constant (Savage and Hutter, 1989; Bartelt et al., 1999; Iverson and Denlinger, 2001; Denlinger and Iverson, 2001).

2.2 Governing Equations and Boundary Conditions - Ali

Starting with the basic conservation of mass and momentum for an incompressible medium, we can describe the motion of an avalanching mass:

$$\begin{aligned} \nabla \cdot \underline{\mathbf{u}} &= 0, \\ \frac{\partial}{\partial t}(\rho\, \underline{\mathbf{u}}) + \nabla \cdot (\rho\, \underline{\mathbf{u}} \otimes \underline{\mathbf{u}}) &= \nabla \cdot \underline{\underline{\mathbf{T}}} + \rho\, \underline{\mathbf{g}}, \end{aligned} \tag{1}$$

Where $\underline{\mathbf{u}} = [u, v, w]^{\mathrm{T}}$, is the material velocity vector, ρ is its constant density, $\underline{\underline{\mathbf{T}}}$ is the *Cauchy* stress tensor, and $\underline{\mathbf{g}}$ is the gravity vector. Based on the material rheology we choose, the Cauchy stress tensor, $\underline{\underline{\mathbf{T}}}$, is defined differently (Freundt and Bursik, 1998). Defining the free and basal surface interfaces respectively as follows,

$$\begin{aligned} F^s(x, y, t) &= s(x, y, t) - z, \\ F^b(x, y, t) &= b(x, y, t) - z, \end{aligned} \tag{2}$$

Therefore, one can impose the *kinematic boundary conditions* at free and basal surface interfaces:

$$\frac{\partial F^s}{\partial t} + \underline{\mathbf{u}} \cdot \nabla F^s = 0, \quad at\ F^s(x, y, t) = 0 \tag{3}$$

$$\frac{\partial F^b}{\partial t} + \underline{\mathbf{u}} \cdot \nabla F^b = 0, \quad at\ F^b(x, y, t) = 0 \tag{4}$$

According to the 2nd and 7th assumptions, we may also impose the traction-free boundary condition at the free surface, while a *Coulomb dry-friction* sliding law at the interface between the granular flow and the basal surface is imposed:

$$\underline{\underline{\mathbf{T}}}^s \underline{n}^s = \underline{0}, \quad at\ F^s(x, y, t) = 0 \tag{5}$$

$$\underline{\underline{\mathbf{T}}}^b \underline{n}^b - \underline{n}^b(\underline{n}^b \cdot \underline{\underline{\mathbf{T}}}^b \underline{n}^b) = \frac{\underline{\mathbf{u}}^b}{\|\underline{\mathbf{u}}^b\|}(\underline{n}^b \cdot \underline{\underline{\mathbf{T}}}^b \underline{n}^b)\mu_{\mathrm{Bed}}, \quad at\ F^b(x, y, t) = 0 \tag{6}$$

where μ_{Bed} is the basal friction coefficient and the basal and surface unit normals are:

$$\underline{n}^b = \frac{\nabla F^b}{\|\nabla F^b\|}, \quad \underline{n}^s = \frac{\nabla F^s}{\|\nabla F^s\|}. \tag{7}$$

It is worth mentioning that $\underline{\underline{\mathbf{T}}}\ \underline{n}$ is a resisting traction, while $\underline{n} \cdot \underline{\underline{\mathbf{T}}}\ \underline{n}$ is the normal pressure and $\underline{n} \cdot \underline{\underline{\mathbf{T}}} - \underline{n}(\underline{n} \cdot \underline{\underline{\mathbf{T}}}\ \underline{n})$ is the resulting shear traction. Considering Equation (6), Coulomb dry-friction sliding law expresses that the magnitude of the basal shear stress is equal to the normal basal pressure multiplied by the basal friction coefficient, μ_{Bed}. Furthermore, Equation (6) is stating that the shear traction is assumed to point in the opposite direction to the basal velocity, $\underline{\mathbf{u}}^b$ (resisting shear traction) which also implicitly assumes that $\underline{\mathbf{u}}^b \cdot \underline{n}^b = 0$ when we also consider the basal kinematic boundary condition.

2.3 Models

3 UQ Process - Andrea

The key purpose of this study is to present a procedure for the improved exploration and quantitative comparison of physical models and their assumptions through the collection of full statistical data. Models are not black boxes, behind each physical model there are different physical assumptions, and therefore it would be more appropriate to look at those instead than at the entire model results. Our statistical approach enables a first step towards a data driven selection of the best modeling assumptions to use.

In particular, a good forecasting capability in the context of mass flows requires the careful selection of the pair $(M(A), P(M(A)))$, where A is a set of assumptions, $M(A)$ is the model which combines those assumptions, and $P(M)$ is a probability distribution in the parameter space of M. An assumption is a quite general concept - for example it can be a specific equation for the internal stress, the implementation of bed curvature effects, of active-passive material stretching, or the use of a specific correction on the pressure effects, etc... Assumptions are what makes the models being different, and each model may be seen as the combined result of a set of assumptions. Sometimes a good model contains a useless assumption that may be removed, sometimes a good assumption should be implemented inside a different model - those are usually considered as subjective choices, not data driven. Moreover, the correct assumptions may change through time, making the analysis more difficult.

It is worth mentioning that whereas the support of $P(M)$ can be restricted to a single point in case an optimization procedure is performed for the reconstruction of a particular flow, this is not possible if we are interested in the general predictive capabilities of the model, i.e. what is desired in probabilistic hazard assessment. In this study we will always assume $P(M) \sim \bigotimes_{i=1}^{N_M} Unif(a_{i,M}, b_{i,M})$, where N_M is the number of parameters of M. These parameter ranges will not be selected under the influence of a particular observation, but we will try to use the information gathered in literature about the physical meaning of those values.

In general, the simulation algorithms can be classified as:

(1)INPUT VARIABLES $\longrightarrow$ (2)DYNAMICAL QUANTITIES $\longrightarrow$ (3)OBSERVABLE OUTPUTS

The input variables can include: volume, rheology coefficients, initiation site and geometry, digital elevation map. We will focus on the former two of those, the volume of the pile and the rheology, which constitute our parameter space in all the case studies. The dynamical quantities are directly related to the force terms in the Newton Equations that rule the simulation, they include: driving and dissipative stresses and powers. The terms of the equations are hidden to the observation, but they directly depend on the parameters, and represent a fundamental link between the parameters and the observable outputs. Moreover, the models share some of those terms while change others, and this enables a detailed comparison of the real physics below the curtain. Finally, the observable outputs include: flow height, inundated area, flow velocity and acceleration. In the sequel (2) and (3) are also called quantities of interest (QoI).

Another level of complexity can be achieved choosing the degree of integration of (2) and (3) in the previous scheme:

(A) LOCAL MEASUREMENTS

(B) SPATIAL AVERAGES

(C) TEMPORAL AVERAGES

(D) SPATIO-TEMPORAL (FULL) AVERAGES

In particular, all the dynamical quantities, and most of the observable outputs, have a local meaning. They are calculated on the elements of the numerical mesh created by the code. Moreover, all those quantities are time dependent. Differences in time and location enable to constrain the changes in flow regime. Those are really important because if the flow behavior is radically different, then the significance and effects of the assumptions may also change.

A first approach to look at the data is to choose a reasonable design of spatial locations and to calculate the graph of the quantities as a function of time. A second approach is to make the spatial integral of those quantities and calculate their temporal graph - this integration can be done with respect to the basal area, e.g. for the stresses and related powers, or with respect to the flow volume, e.g. velocity and acceleration. A third possible approach requires to make the integrals through time at each designed spatial site, a fourth approach the full integral in space-time.

In general, for each QoI and degree of integration, during a Monte Carlo simulation we sample the input variables and obtain a family of temporal graphs in (A), (B), and numeric values in (C), (D). These results are statistically summarized - plotting their expectation, their standard deviation, their 5th and 95 percentiles. Their correlation structure is also explored, presenting the plots of the Pearson coefficients of the most interesting pairs of quantities in (1), (2), (3). In the following, we will detail the considered input variables and quantities of interest for each of our cases study.

Our sampling technique of the input variables is based on the Latin Hypercube Sampling (LHS) idea, and in particular, on the improved space-filling properties of the orthogonal array-based Latin Hypercubes (see Appendix A). The LHS is performed over $[0,1]^3$ for the MC and VS input parameters, and $[0,1]^4$ for PF input parameters. Those samples are homothetically transformed to fill the required intervals.

3.1 Definition and consistency of the Input parameters - Andrea + Ali

In general, the three rheologies considered in this study, MC, PF, and VS, have different parameters, but in all them it is defined a basal friction stress F. That is $F = \tan(\phi_{bed})$ in MC, $F = \tan(\phi_2)$ for $Fr \gg h$ in PF, $F = \mu$ in VS. We use those relations to define parameter spaces which produce reasonably consistent ranges of basal frictions. In the following sections, we start defining a range for ϕ_{bed} of MC, specific of the scenario and obtained from the more rich literature of that rheology, then we impose a consistent range for the related parameters of PF and VS, and leave the other parameters unchanged. In particular:

MC

$\phi_{bed} \in [a, b]$, depending on the case study.
$\phi_{int} - \phi_{bed} = \Delta\phi \in [2, 10]$, following Dalbey et al. (2008), but 25% enlargement on the higher side of the uncertainty range.

PF

$\phi_2 = \phi_{bed}$, but with $\sim$20% enlargement on the higher side of the uncertainty range.
$\phi_2 - \phi_1 = \Delta\phi_{12} \in [5, 15]$ (Gray and Edwards (2014) used 9 degrees, Barker et al. (2015) 11 degrees).
$\beta \in [0.1, 0.85]$ (Gray and Edwards (2014) assumed $\beta = 0.14$, Forterre and Pouliquen (2003) $\beta = 0.65$)
$L = 10^{-3}$, $\phi_3 = 35$ (Gray and Edwards, 2014) due to their reduced sensitivity (see Appendix B).

VS

$\mu = \tan(\phi_{bed})$, with $\sim$20% enlargement of the uncertainty range.
$\log(\xi) \in [1.7, 4] = \log[50, 10^4]$, i.e. in this case the uniform sampling is accomplished in log-scale.

4 QoIs and Data Collected

4.1 Flow down an inclined plane

The parameter ranges adopted in this case study are:

MC - $\phi_{bed} \in [15^\circ, 30^\circ]$ (Dalbey et al., 2008), $\Delta\phi \in [2^\circ, 10^\circ]$.

PF - $\phi_2 \in [15^\circ, 35^\circ]$, $\Delta\phi_{12} \in [5^\circ, 15^\circ]$, $\beta \in [0.1, 0.85]$, $L = 10^{-3}\ (m)$, $\phi_3 = \phi_1 + 1^\circ$.

VS - $\mu \in [0.2, 0.7]$, $\log(\xi) \in [1.7, 4]$.

4.1.1 Flow Height

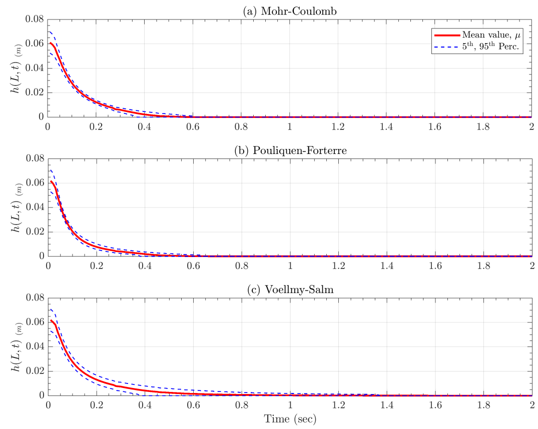

(a) $L = (-0.7, 0)$, slumping pile location.

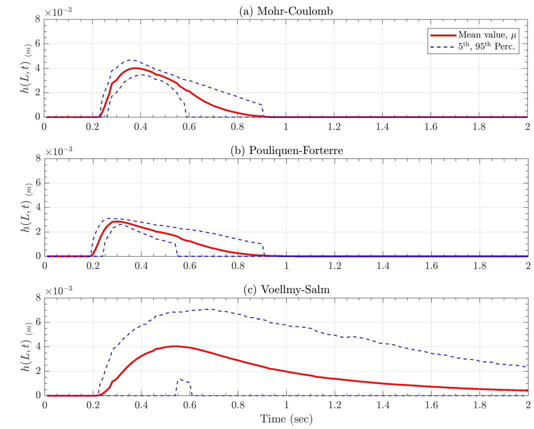

(b) $L = (-0.35, 0)$, middle point on inclined plane.

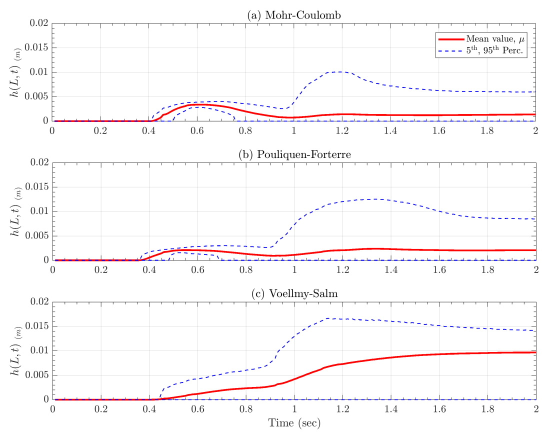

(c) $L = (0, 0)$, inclined and runout planes' joint location.

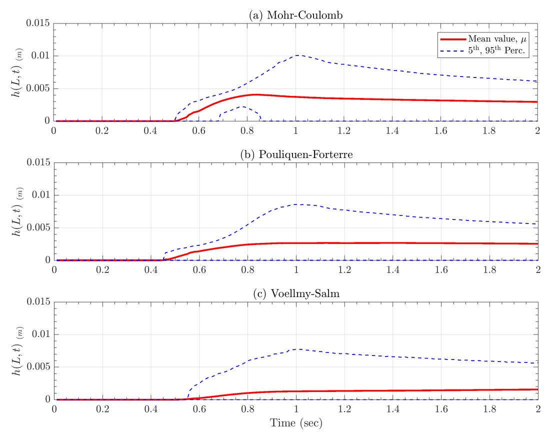

(d) $L = (0.15, 0)$, a location on runout plane.

Figure 3: Records of flow height, $h(L, t)$.

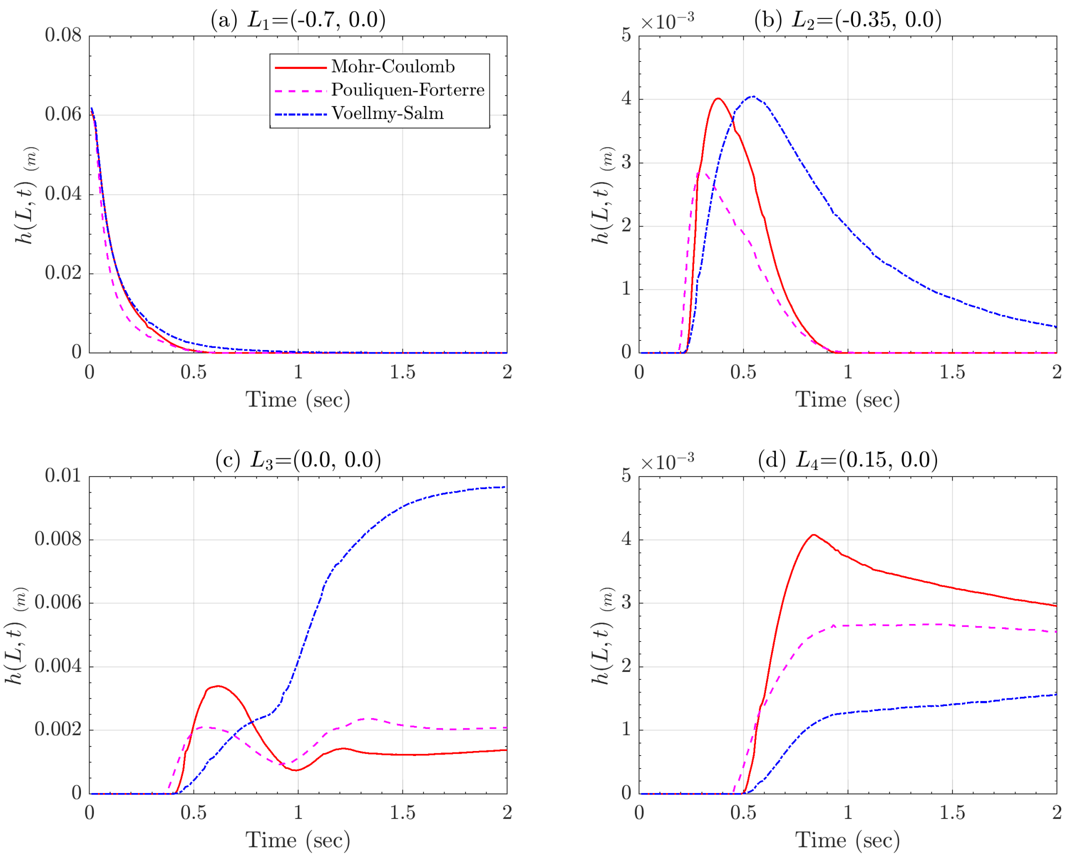

Figure 4: Comparison between mean values of flow height, $h(L, t)$, recorded at locations of interest, L_i, ${}_{i=1,\ldots,4}$.

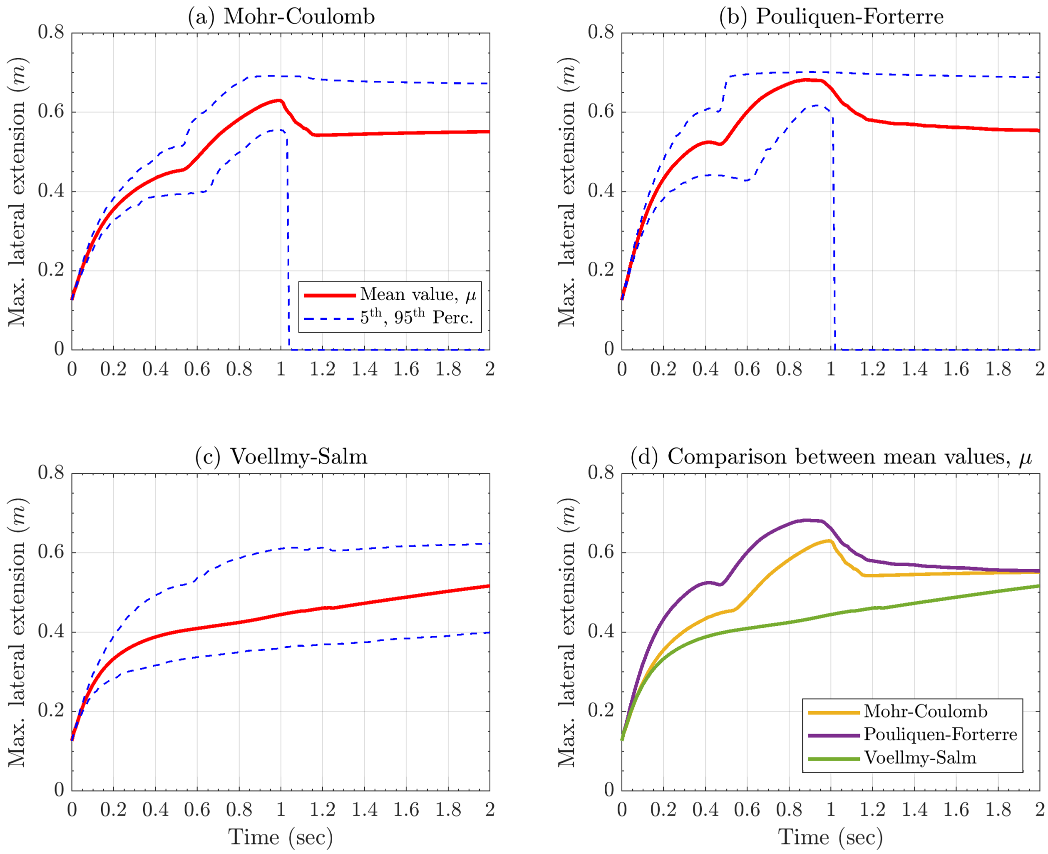

Figure 5: Comparison between mean values of flow height recorded at locations of interest, L_i, $_{i=1,\ldots,4}$.

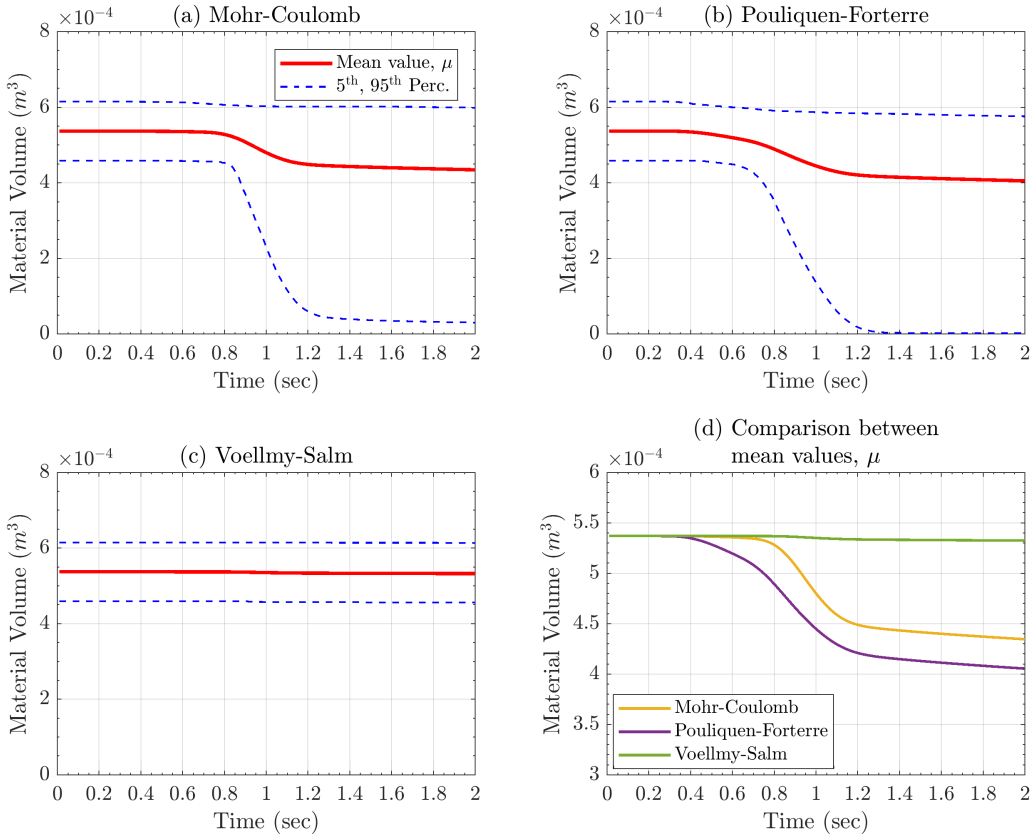

Figure 6: Comparison between mean values of flow height, $h(L,t)$, recorded at locations of interest, $L_i,\ _{i=1,\ldots,4}$.

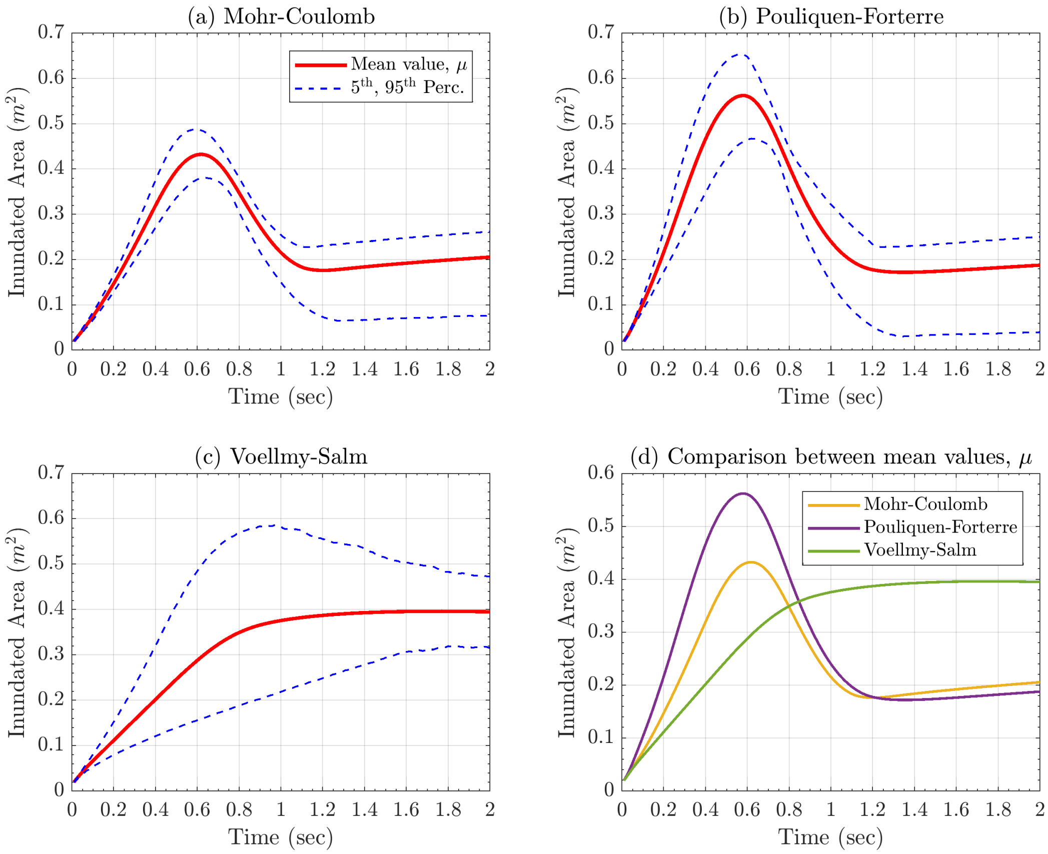

Figure 7: Comparison between mean values of flow height, $h(L, t)$, recorded at locations of interest, $L_i,\ _{i=1,\ldots,4}$.

4.1.2 Flow Velocity

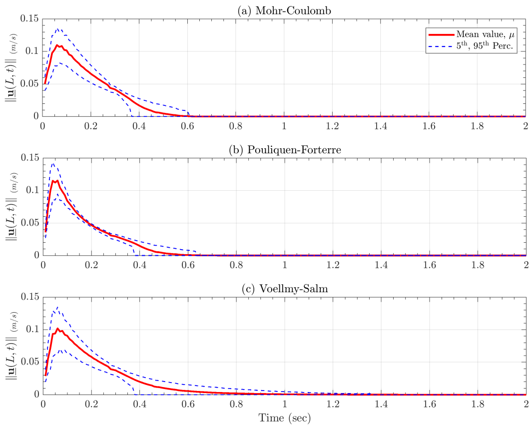

(a) $L = (-0.7, 0)$, slumping pile location.

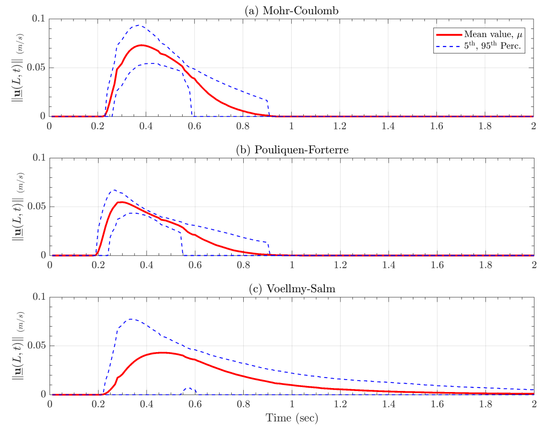

(b) $L = (-0.35, 0)$, middle point on inclined plane.

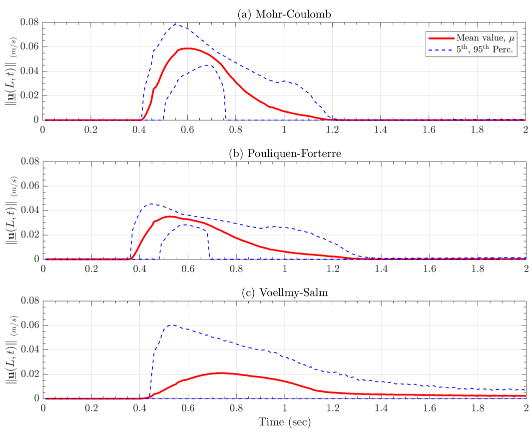

(c) $L = (0, 0)$, inclined and runout planes' joint location.

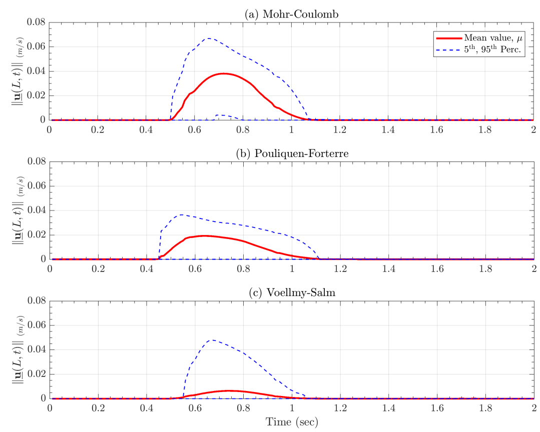

(d) $L = (0.15, 0)$, a location on runout plane.

Figure 8: Records of flow velocity, $\|\underline{\mathbf{u}}\|(L, t)$.

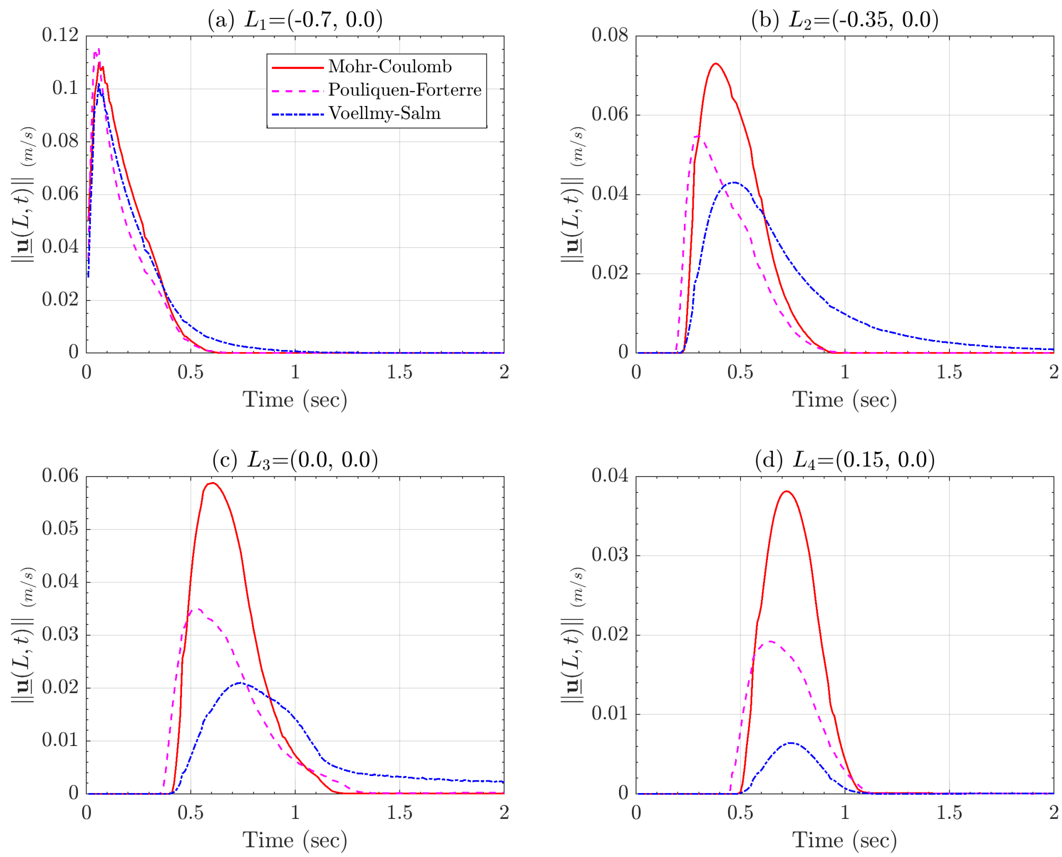

Figure 9: Comparison between mean values of flow velocity, $\|\underline{\mathbf{u}}\|(L,t)$, recorded at locations of interest, $L_i,\ _{i=1,\dots,4}$.

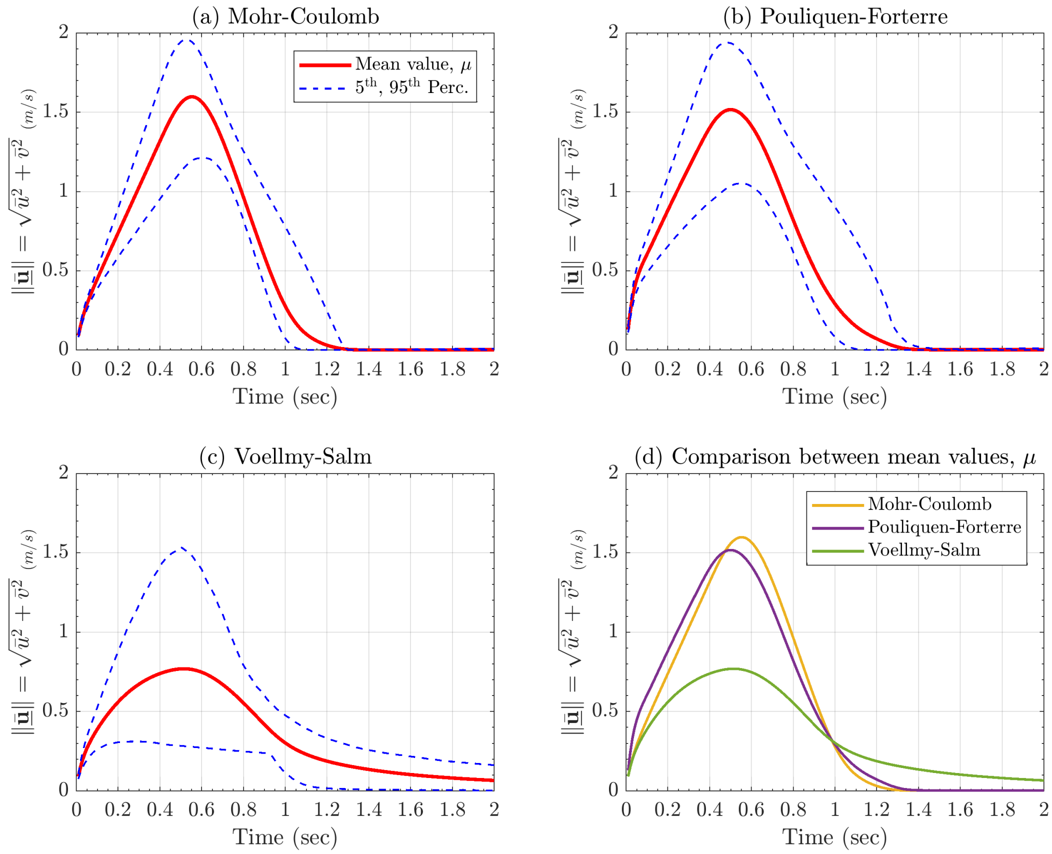

Figure 10: Comparison between mean values of flow velocity, $\|\underline{\mathbf{u}}\|(L,t)$, recorded at locations of interest, $L_i,\ _{i=1,\ldots,4}$.

4.1.3 Froude Number

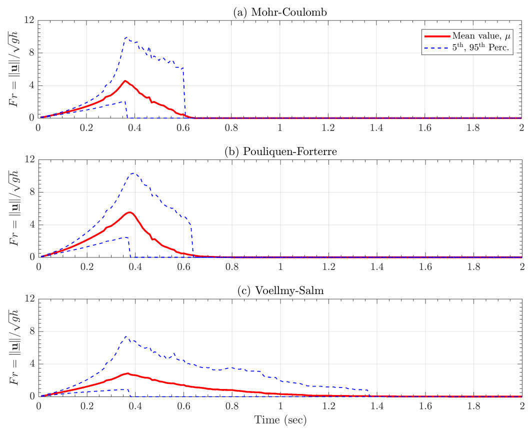

(a) $L = (-0.7, 0)$, slumping pile location.

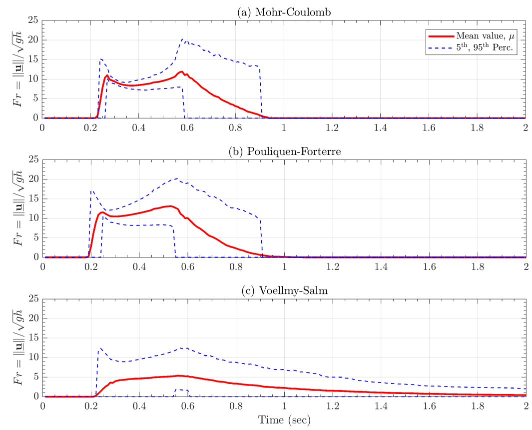

(b) $L = (-0.35, 0)$, middle point on inclined plane.

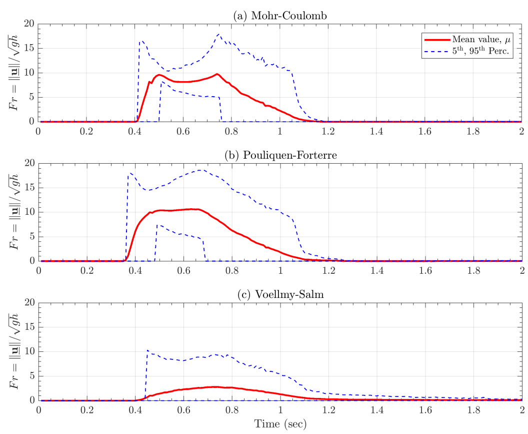

(c) $L = (0, 0)$, inclined and runout planes' joint location.

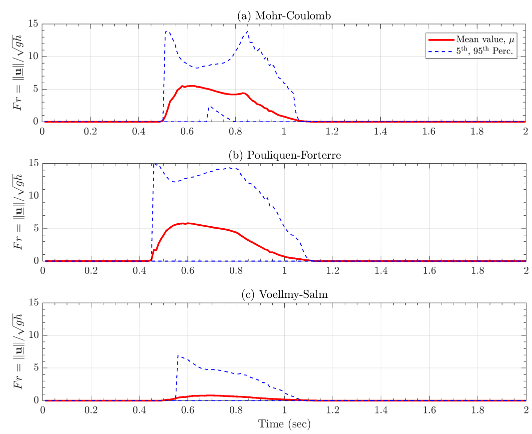

(d) $L = (0.15, 0)$, a location on runout plane.

Figure 11: Records of flow velocity, $\|\underline{\mathbf{u}}\|(L, t)$.

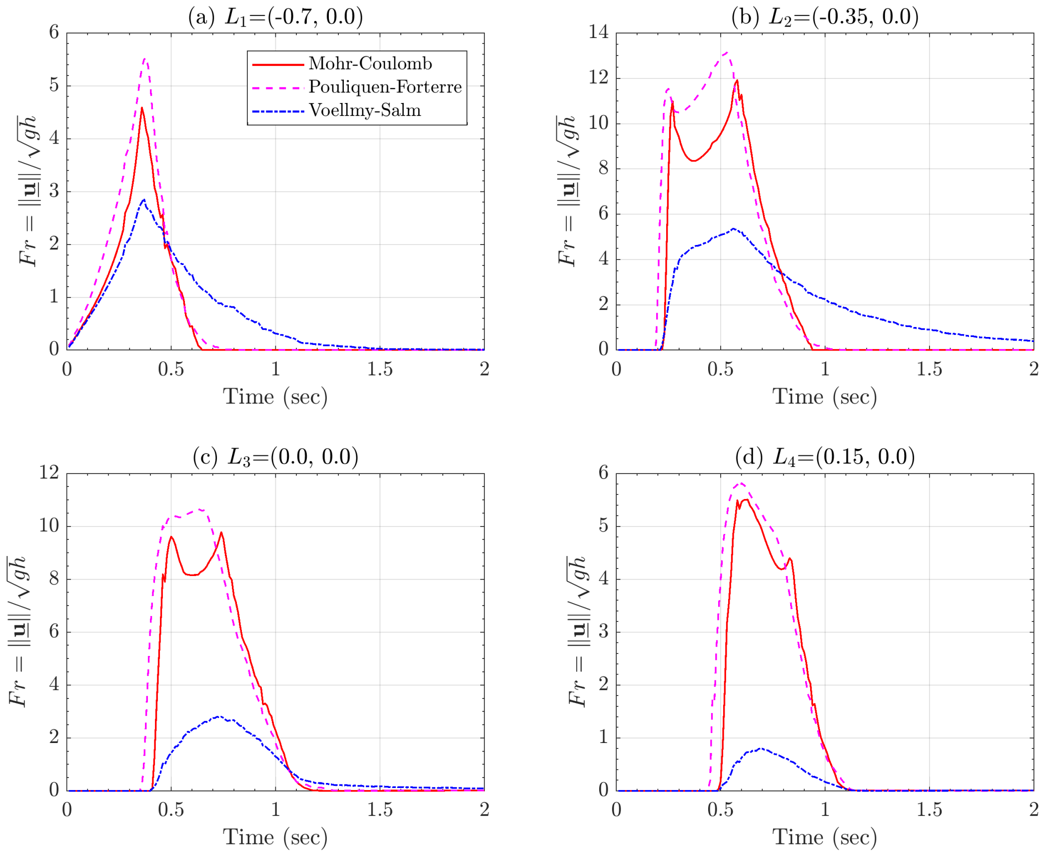

Figure 12: Comparison between mean values of flow velocity, $\|\underline{\mathbf{u}}\|(L,t)$, recorded at locations of interest, L_i, ${}_{i=1,\ldots,4}$.

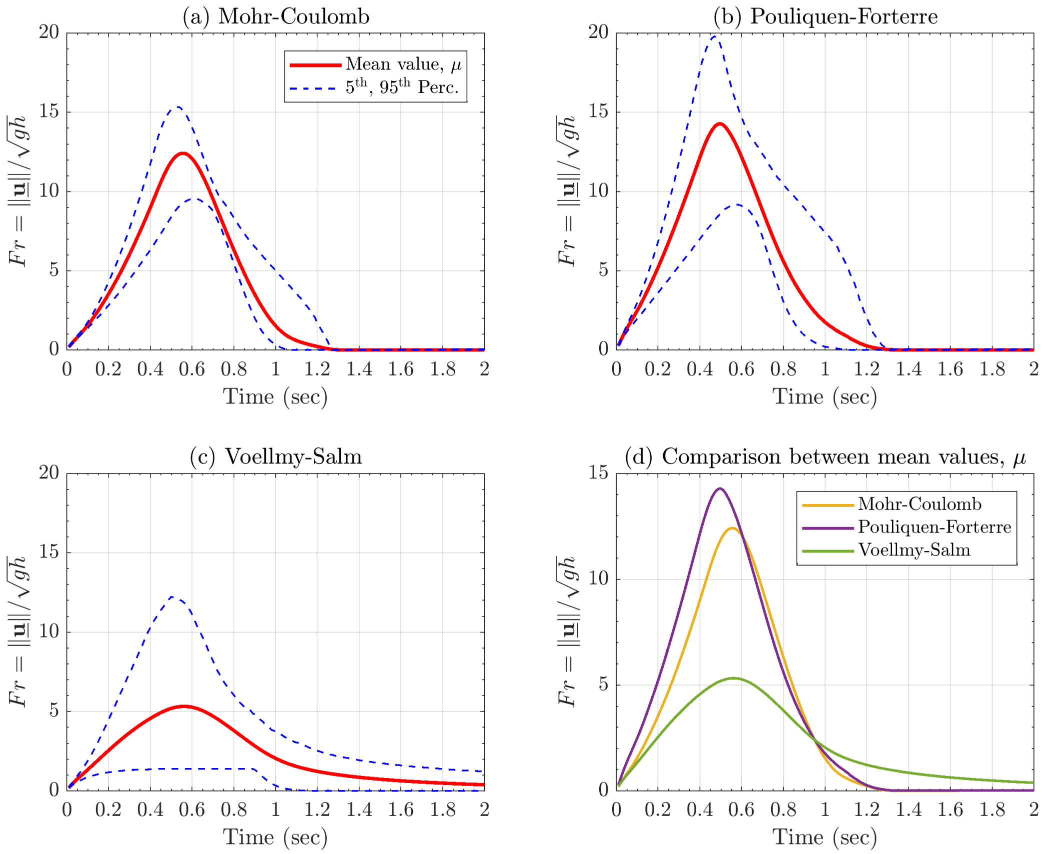

Figure 13: Comparison between mean values of flow velocity, $\|\underline{\mathbf{u}}\|(L, t)$, recorded at locations of interest, $L_i,\ _{i=1,\ldots,4}$.

4.1.4 Flow Acceleration

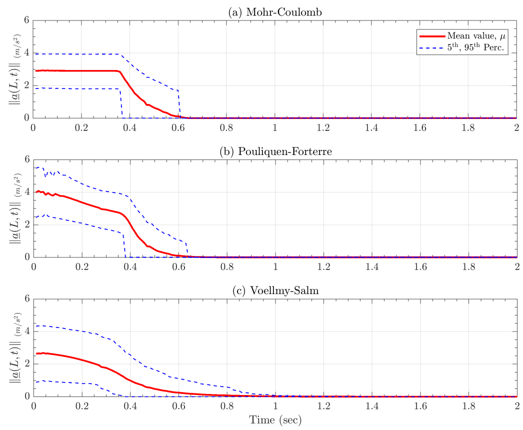

(a) $L = (-0.7, 0)$, slumping pile location.

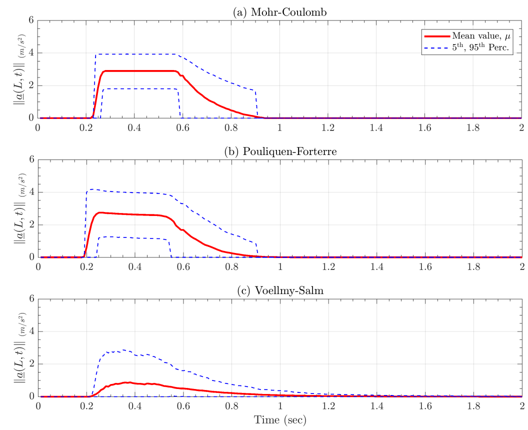

(b) $L = (-0.35, 0)$, middle point on inclined plane.

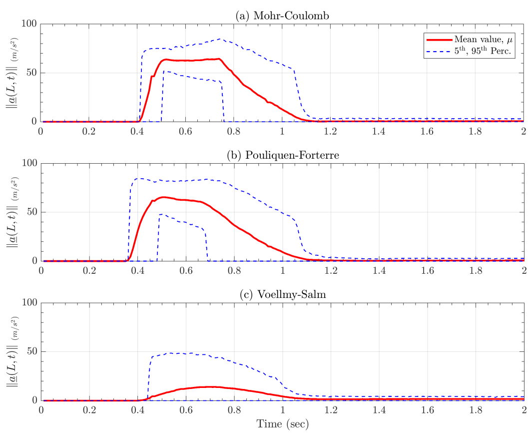

(c) $L = (0, 0)$, inclined and runout planes' joint location.

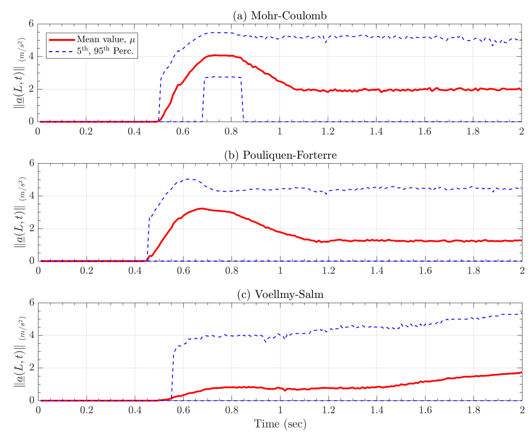

(d) $L = (0.15, 0)$, a location on runout plane.

Figure 14: Records of flow acceleration (computed from RHS), $\|\underline{\mathbf{a}}\|(L, t)$.

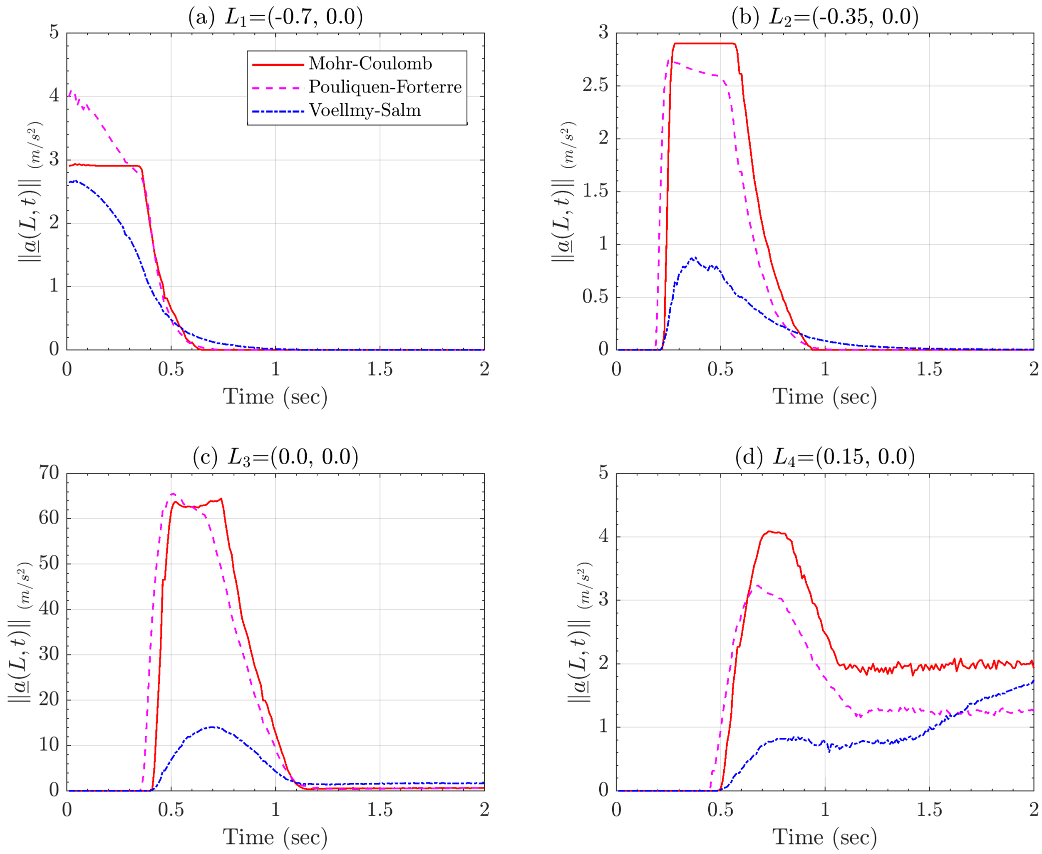

Figure 15: Comparison between mean values of flow acceleration (computed from RHS), $\|\underline{a}\|(L,t)$, recorded at locations of interest, $L_i,\ _{i=1,\dots,4}$.

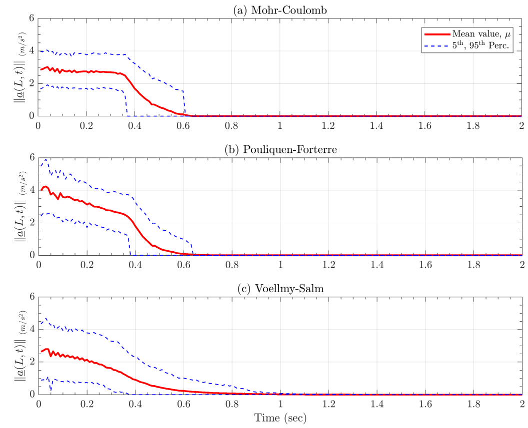

(a) $L = (-0.7, 0)$, slumping pile location.

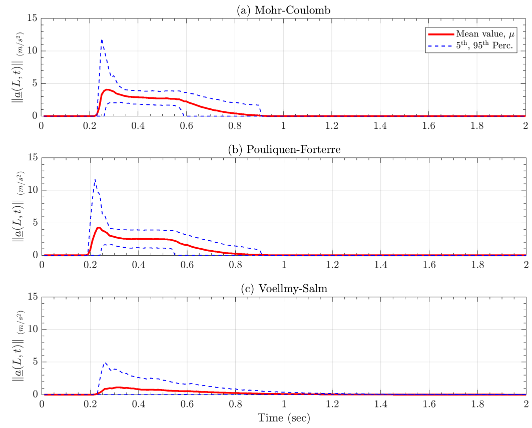

(b) $L = (-0.35, 0)$, middle point on inclined plane.

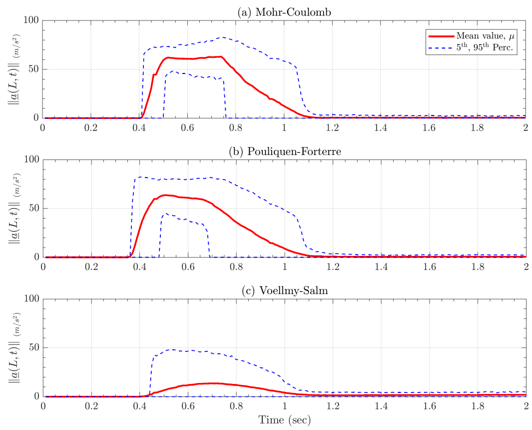

(c) $L = (0, 0)$, inclined and runout planes' joint location.

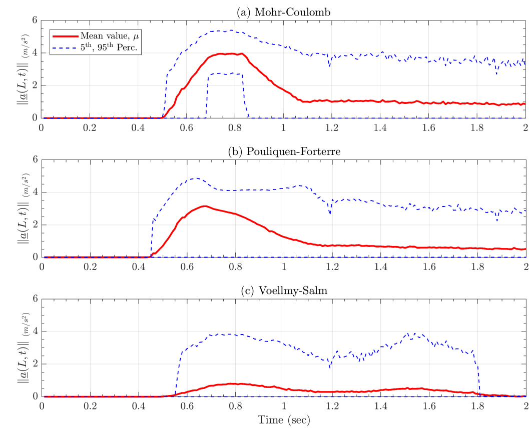

(d) $L = (0.15, 0)$, a location on runout plane.

Figure 16: Records of flow acceleration (computed from LHS), $\|\underline{\mathbf{a}}\|(L, t)$.

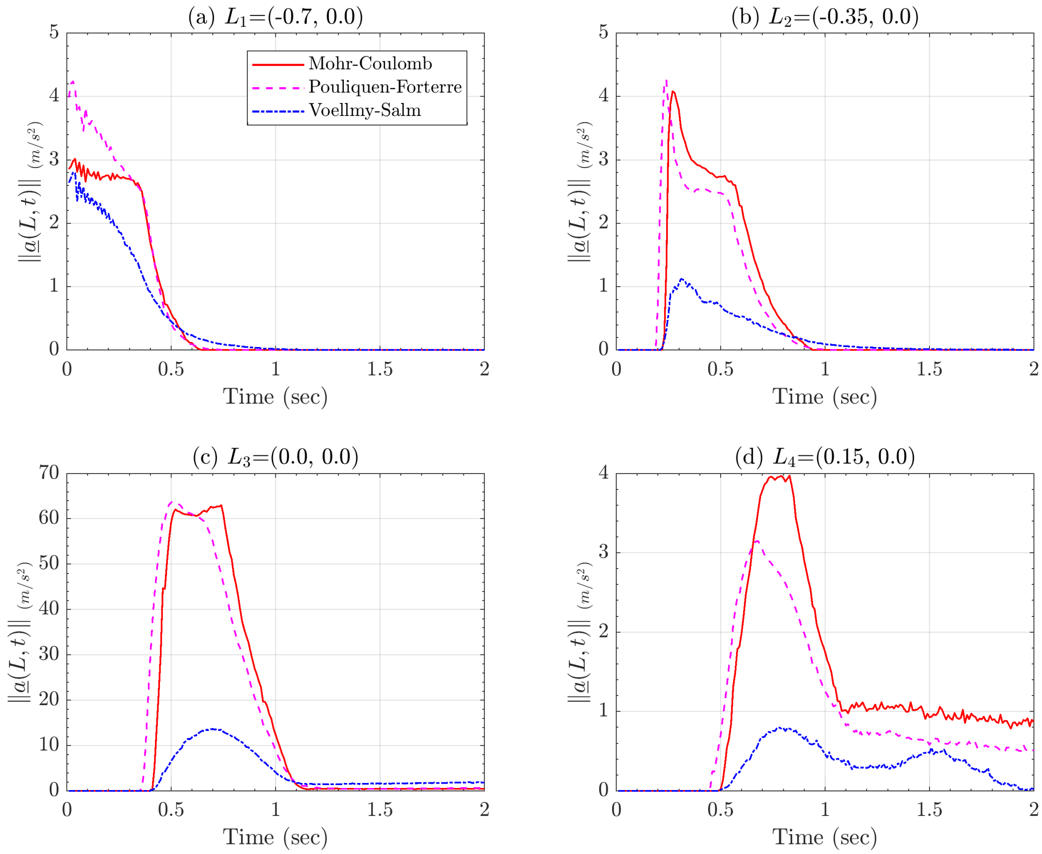

Figure 17: Comparison between mean values of flow acceleration (computed from LHS), $\|\underline{a}\|(L,t)$, recorded at locations of interest, $L_i, \ _{i=1,\ldots,4}$.

4.1.5 Forces and Powers

- **LHS$_1$**

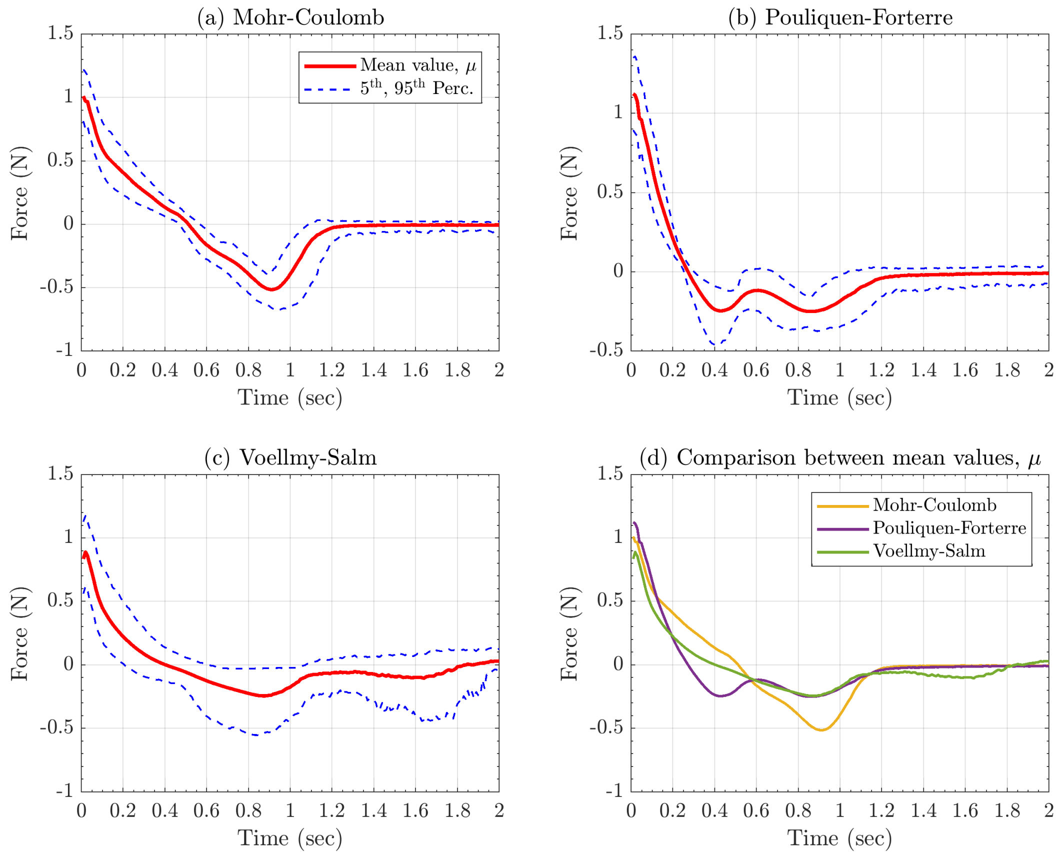

Figure 18: Comparison between mean values of flow acceleration (computed from LHS), $\|\underline{a}\|(L,t)$, recorded at locations of interest, $L_i, \ _{i=1,\ldots,4}$.

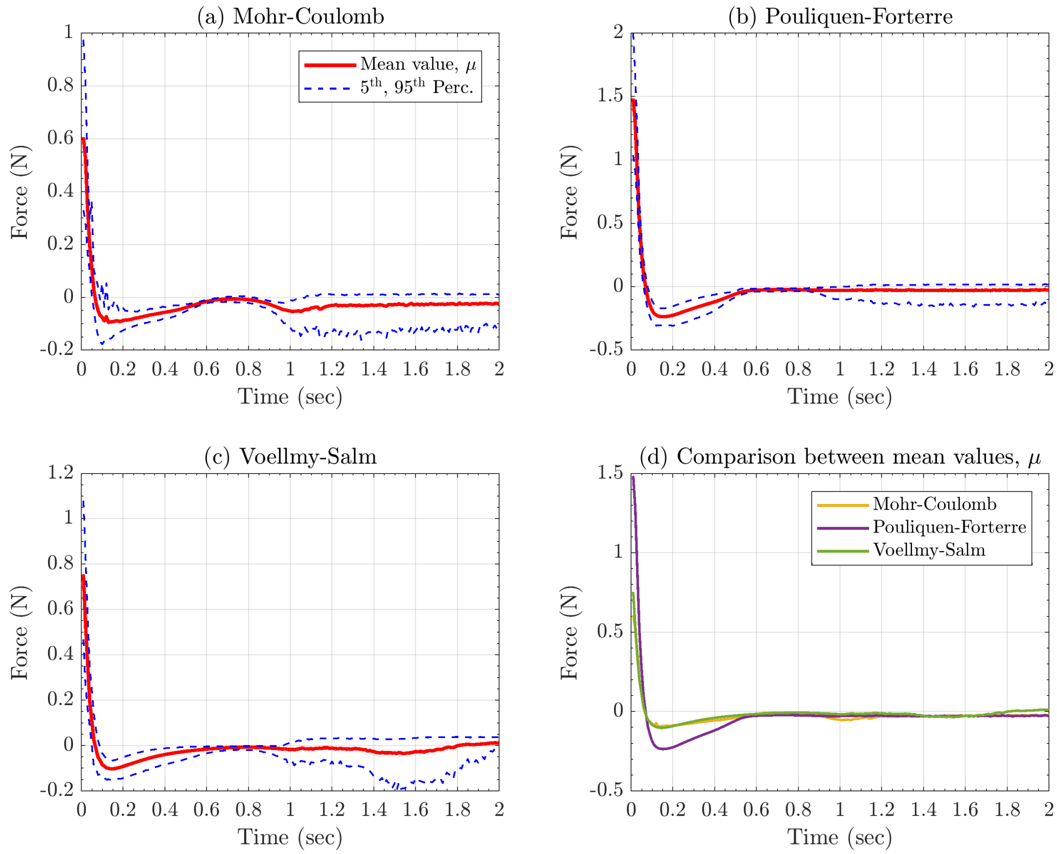

Figure 19: Comparison between mean values of flow acceleration (computed from LHS), $\|\underline{a}\|(L,t)$, recorded at locations of interest, $L_i,\ _{i=1,\ldots,4}$.

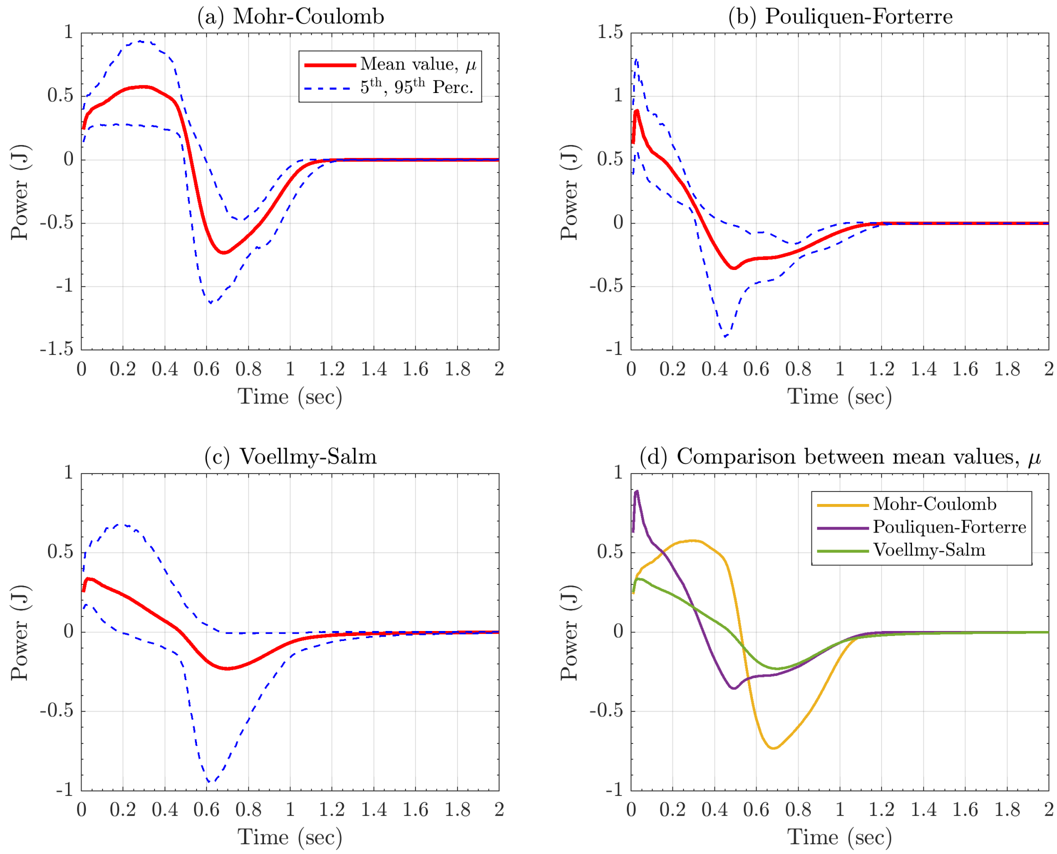

Figure 20: Comparison between mean values of flow acceleration (computed from LHS), $\|\underline{a}\|(L,t)$, recorded at locations of interest, $L_i,\ _{i=1,\ldots,4}$.

- **LHS$_2$**

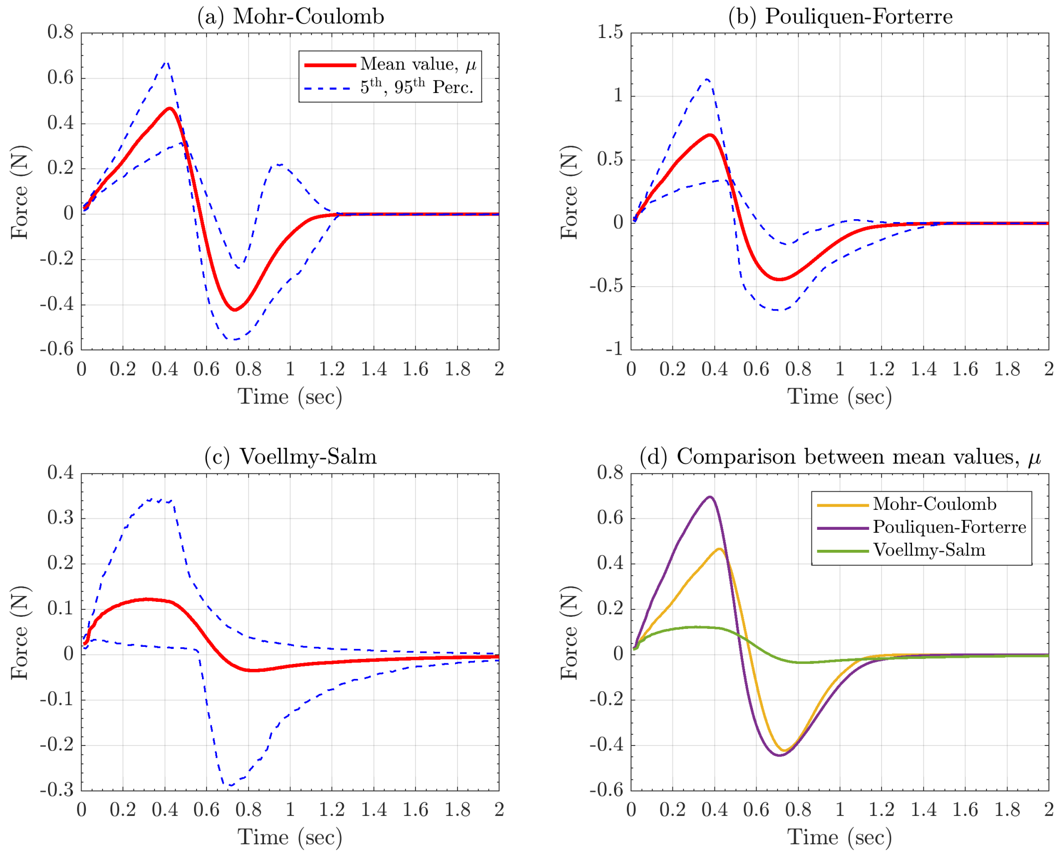

Figure 21: Comparison between mean values of flow acceleration (computed from LHS), $\|\underline{a}\|(L,t)$, recorded at locations of interest, $L_i,\ _{i=1,\ldots,4}$.

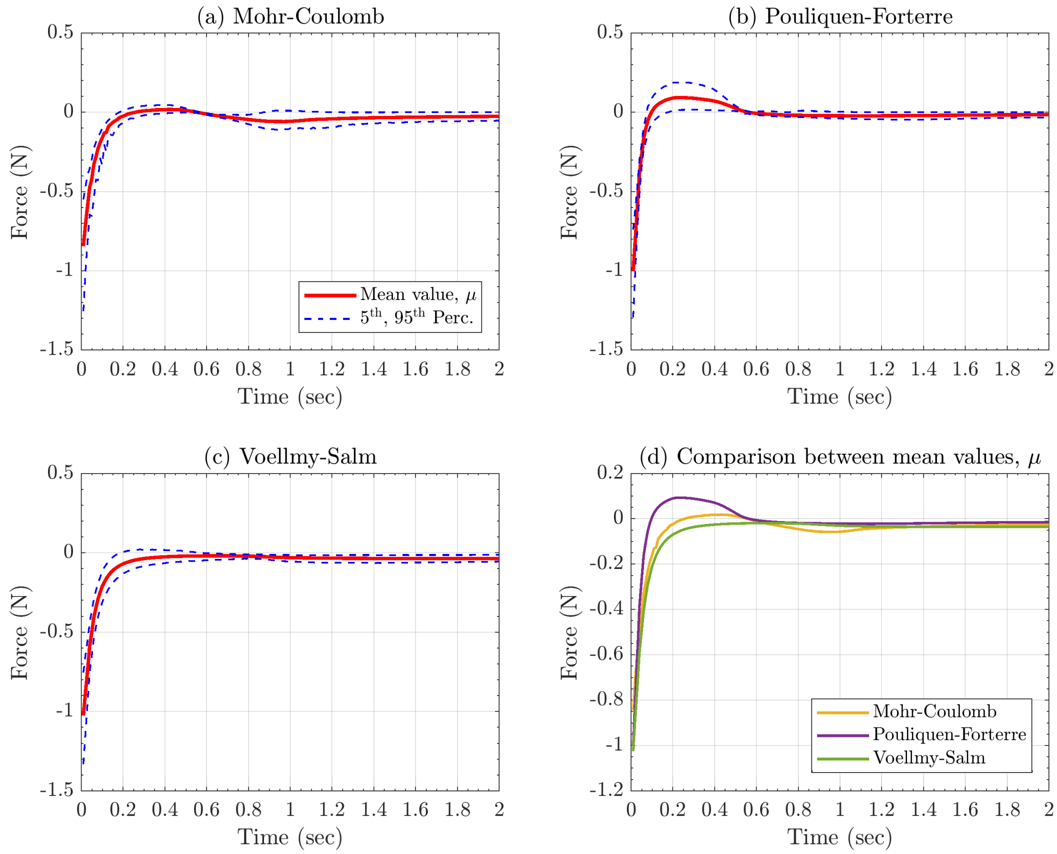

Figure 22: Comparison between mean values of flow acceleration (computed from LHS), $\|\underline{a}\|(L,t)$, recorded at locations of interest, $L_i,\ _{i=1,\ldots,4}$.

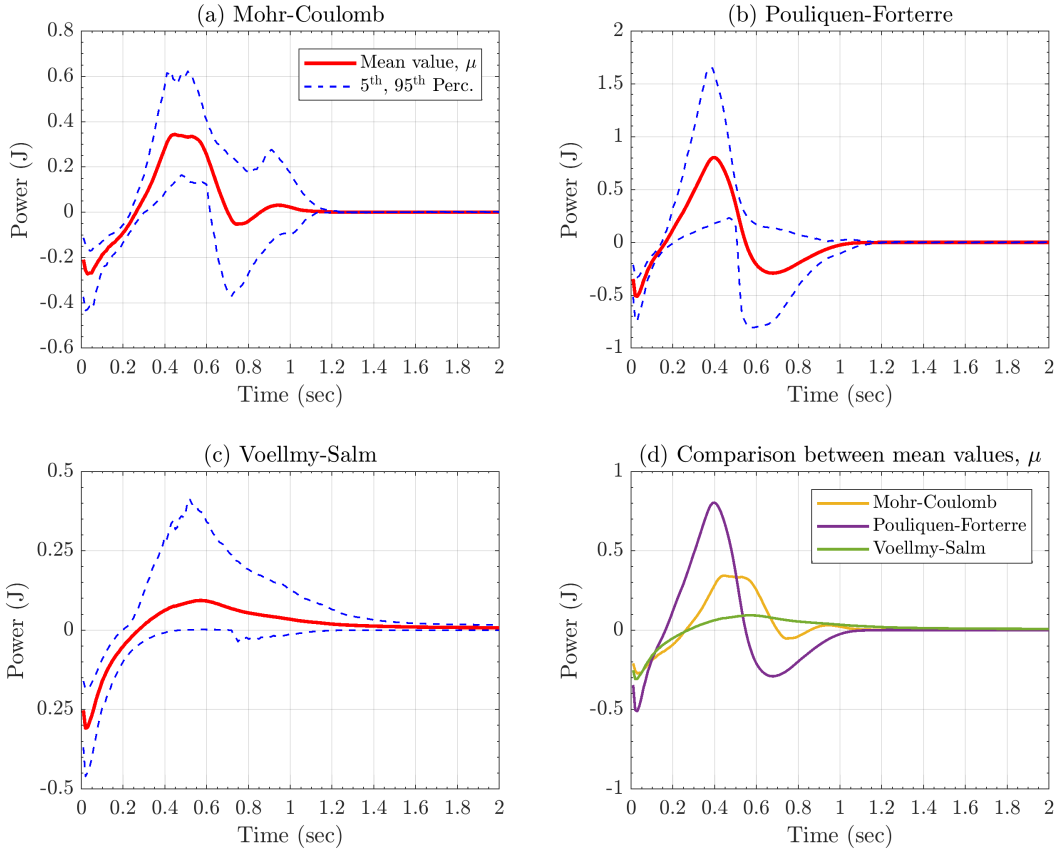

Figure 23: Comparison between mean values of flow acceleration (computed from LHS), $\|\underline{a}\|(L,t)$, recorded at locations of interest, $L_i,\ _{i=1,\ldots,4}$.

- **RHS$_1$**

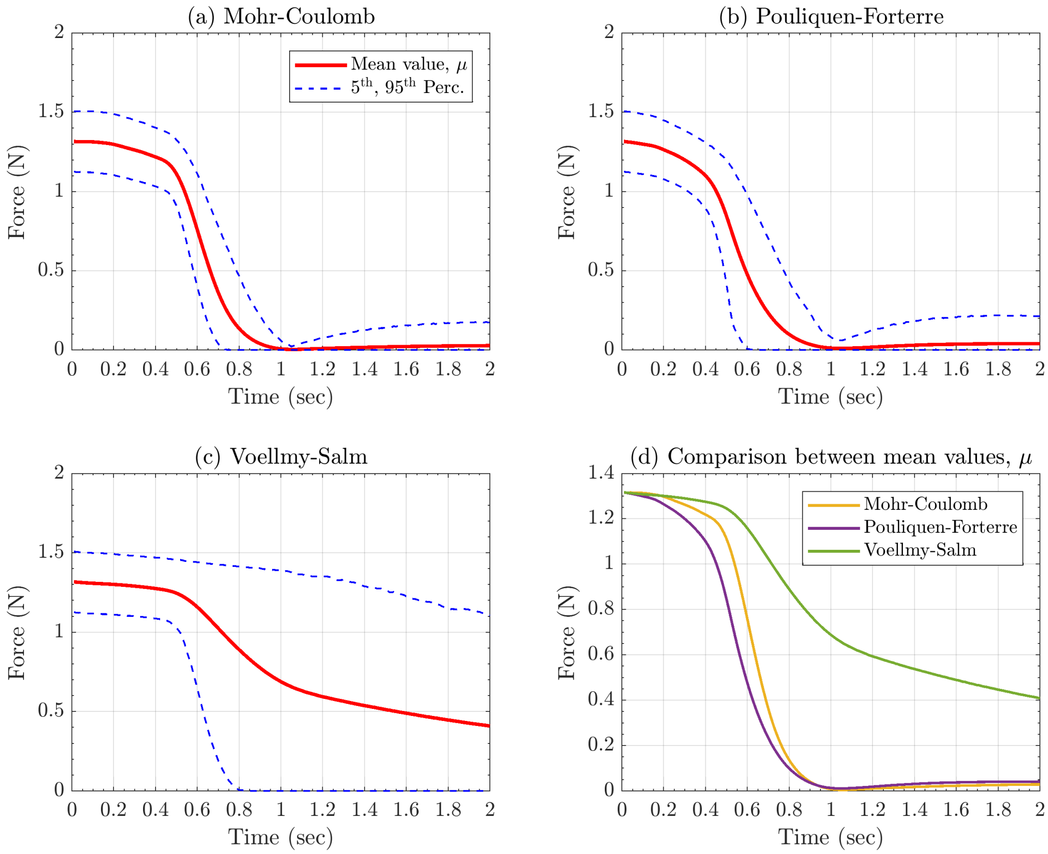

Figure 24: Comparison between mean values of flow acceleration (computed from LHS), $\|\underline{a}\|(L,t)$, recorded at locations of interest, L_i, $_{i=1,\ldots,4}$.

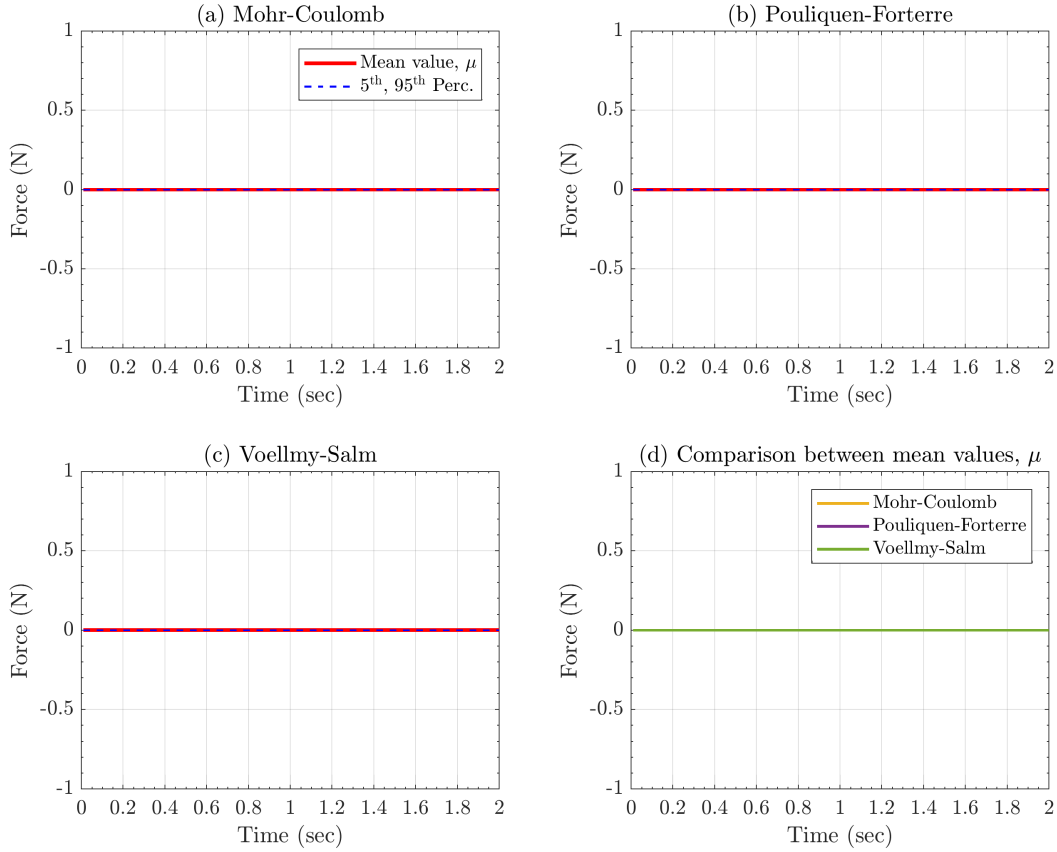

Figure 25: Comparison between mean values of flow acceleration (computed from LHS), $\|\underline{a}\|(L,t)$, recorded at locations of interest, $L_i,\ _{i=1,\ldots,4}$.

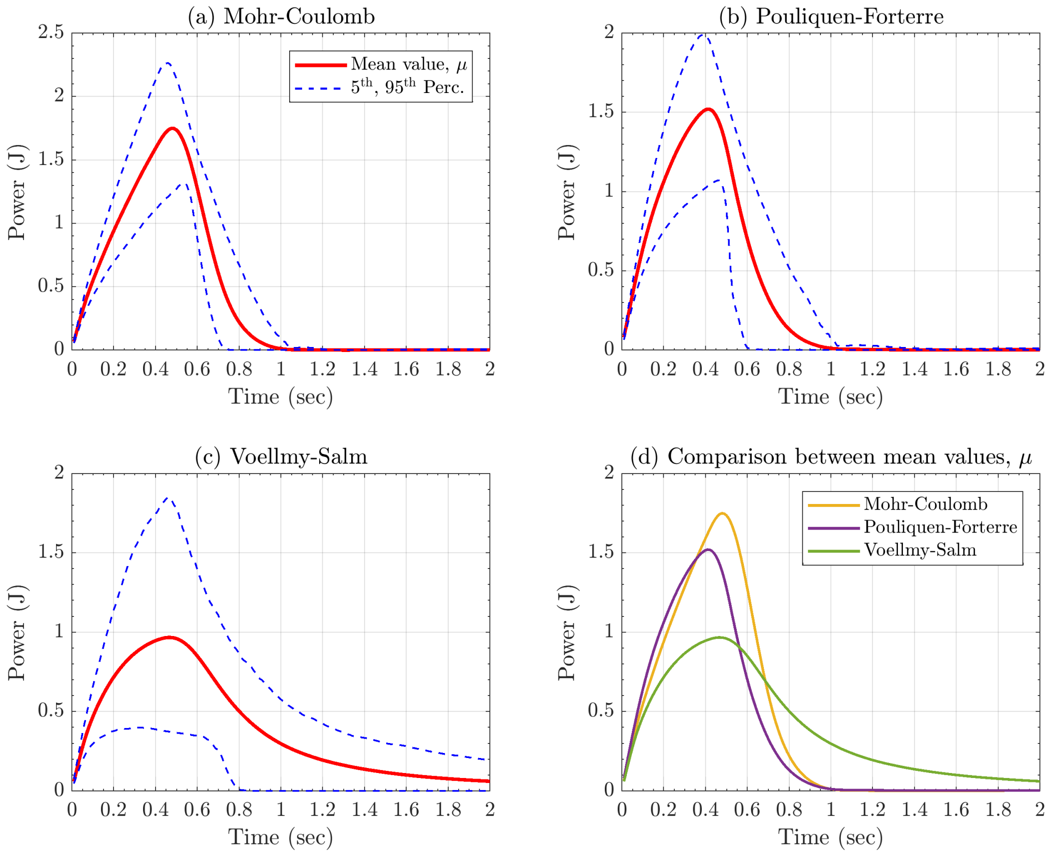

Figure 26: Comparison between mean values of flow acceleration (computed from LHS), $\|\underline{a}\|(L,t)$, recorded at locations of interest, $L_i,\ _{i=1,\ldots,4}$.

• **RHS$_2$**

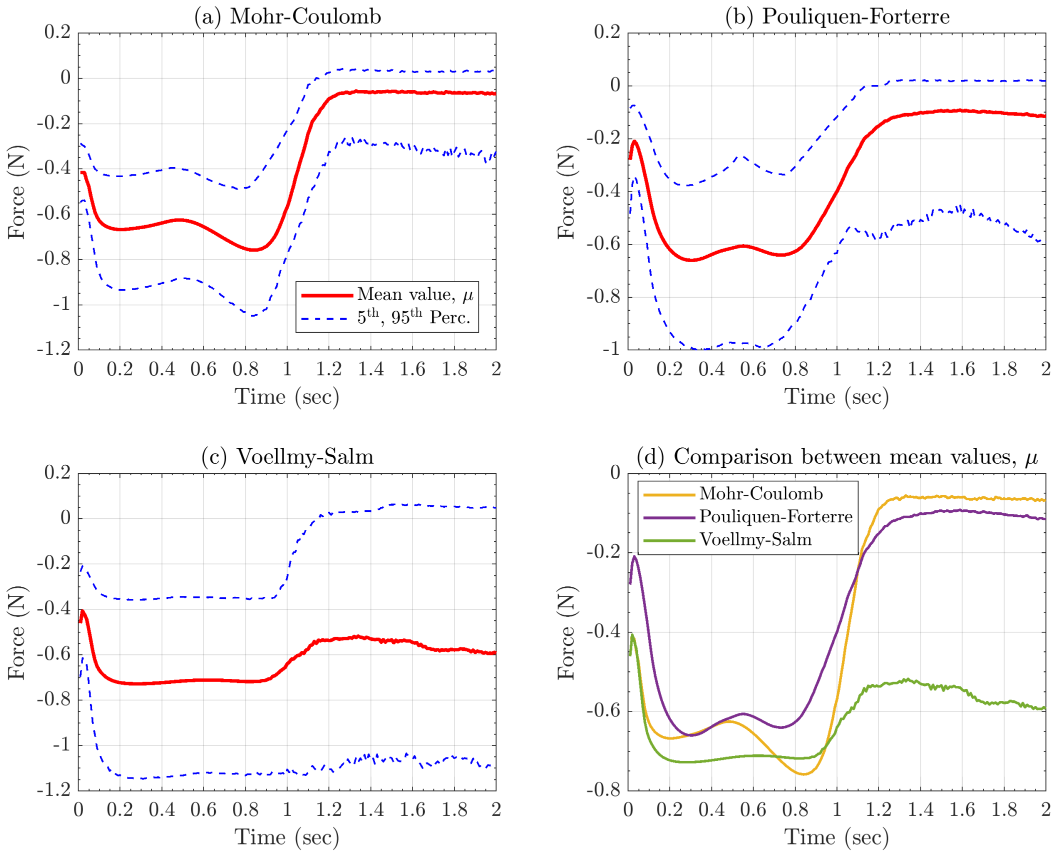

Figure 27: Comparison between mean values of flow acceleration (computed from LHS), $\|\underline{a}\|(L,t)$, recorded at locations of interest, $L_i, \;_{i=1,\ldots,4}$.

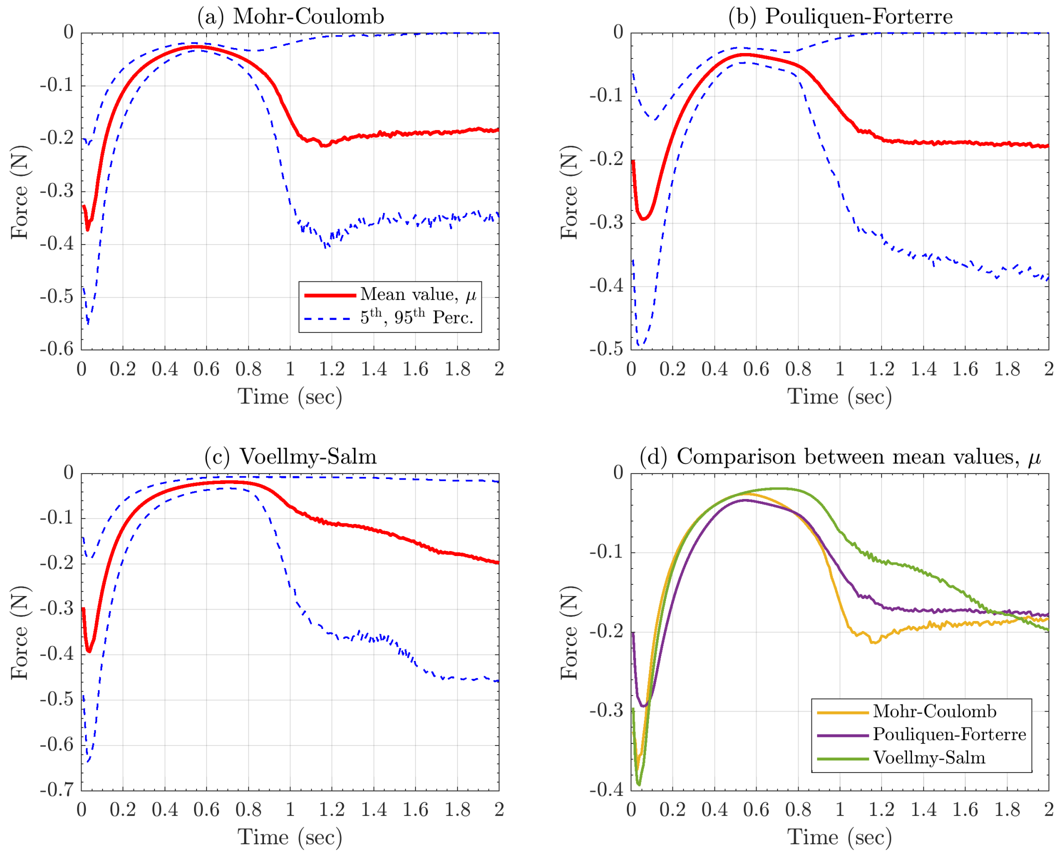

Figure 28: Comparison between mean values of flow acceleration (computed from LHS), $\|\underline{a}\|(L,t)$, recorded at locations of interest, $L_i,\ _{i=1,\ldots,4}$.

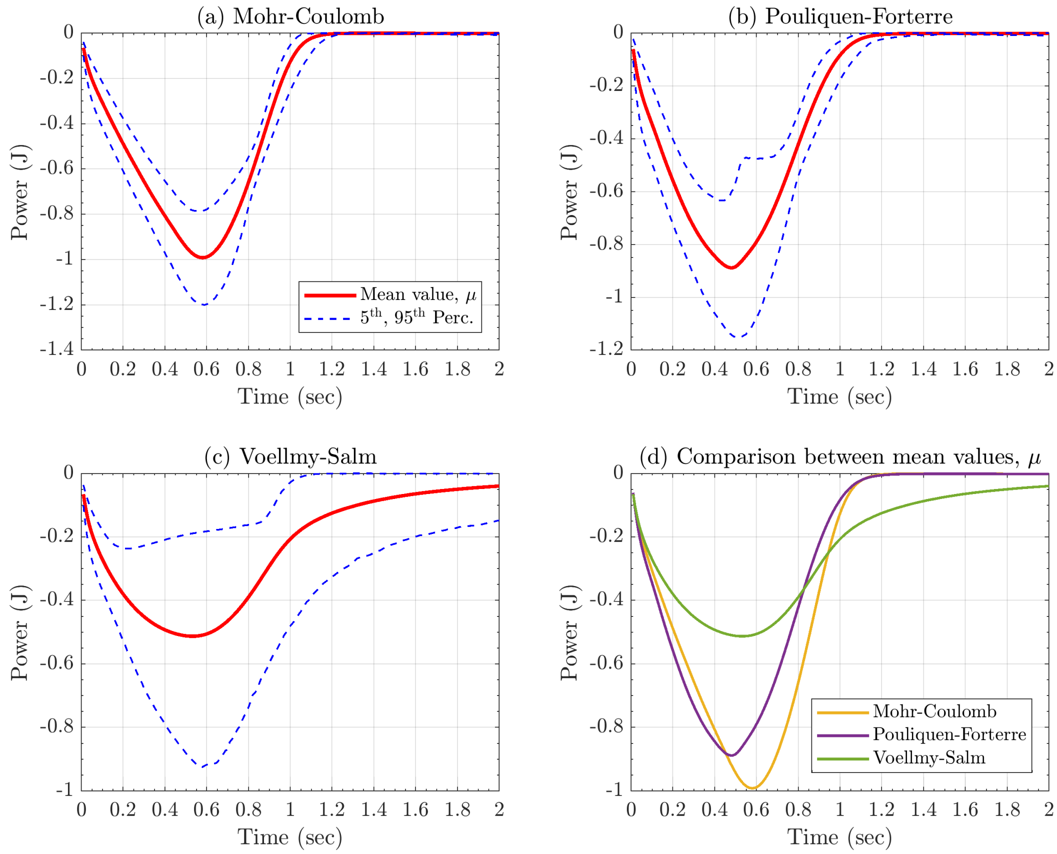

Figure 29: Comparison between mean values of flow acceleration (computed from LHS), $\|\underline{a}\|(L,t)$, recorded at locations of interest, $L_i,\ _{i=1,\ldots,4}$.

- **RHS$_3$**

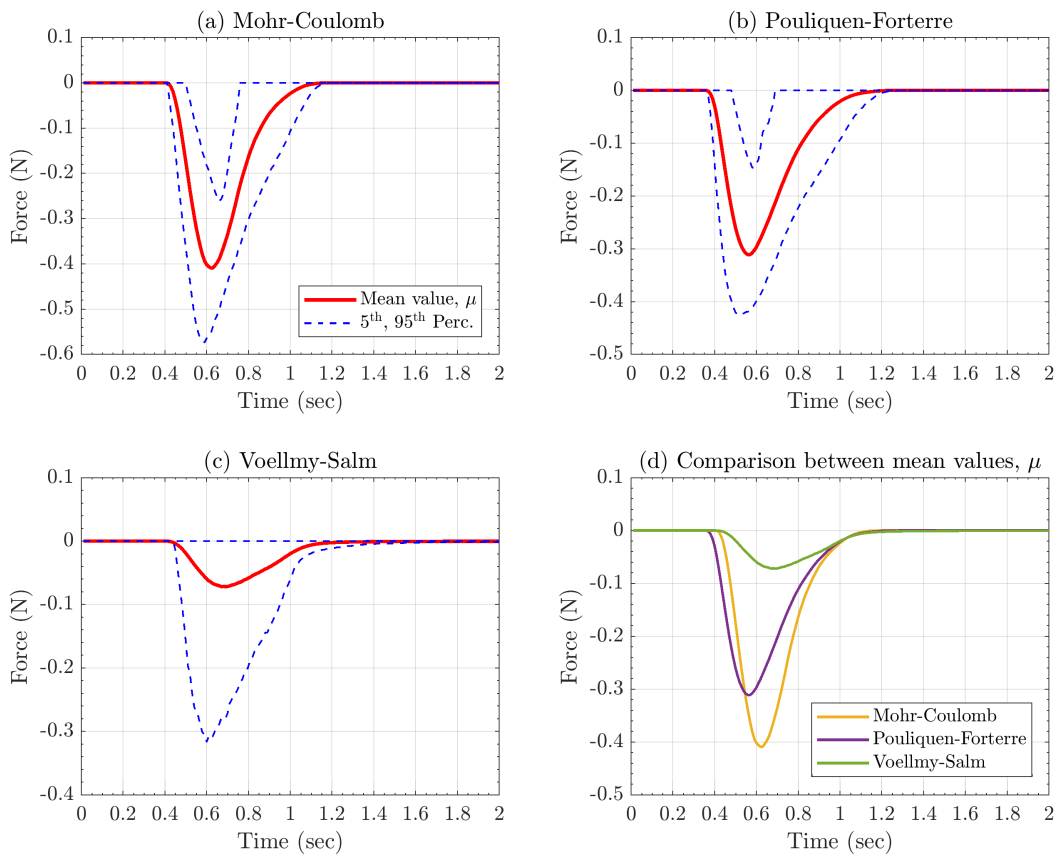

Figure 30: Comparison between mean values of flow acceleration (computed from LHS), $\|\underline{a}\|(L,t)$, recorded at locations of interest, $L_i,\ _{i=1,\ldots,4}$.

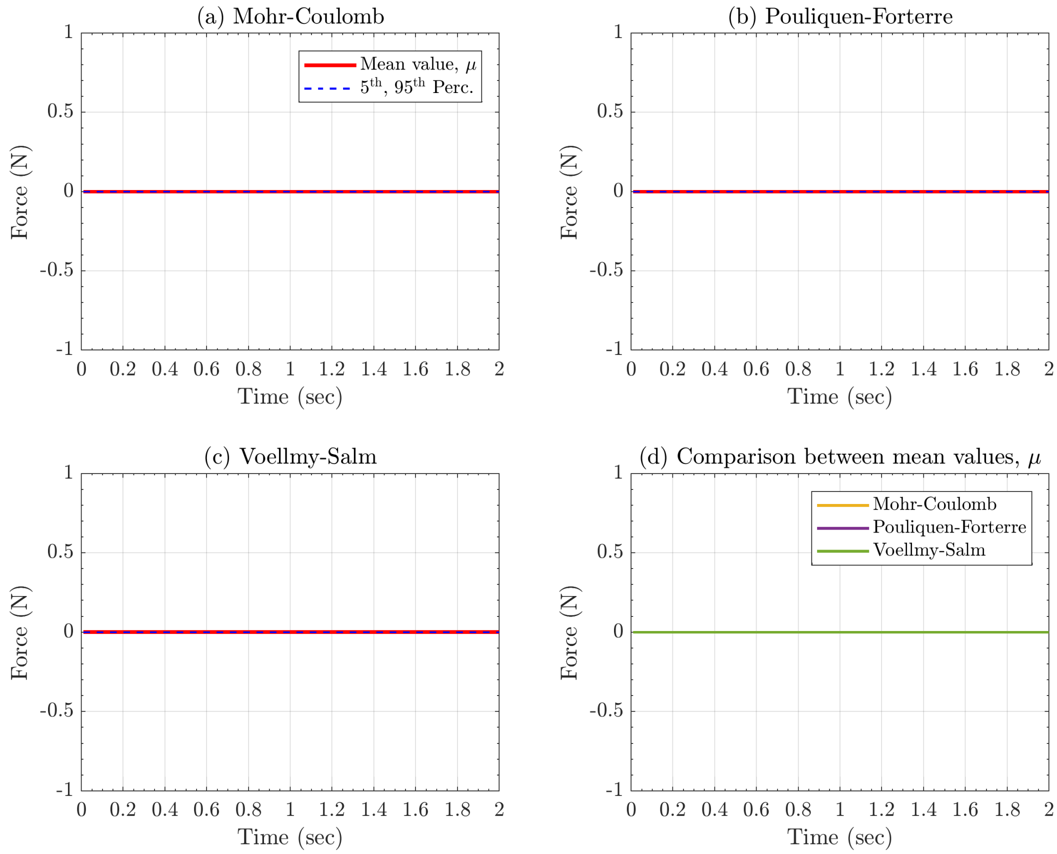

Figure 31: Comparison between mean values of flow acceleration (computed from LHS), $\|\underline{a}\|(L,t)$, recorded at locations of interest, $L_i,\ _{i=1,\ldots,4}$.

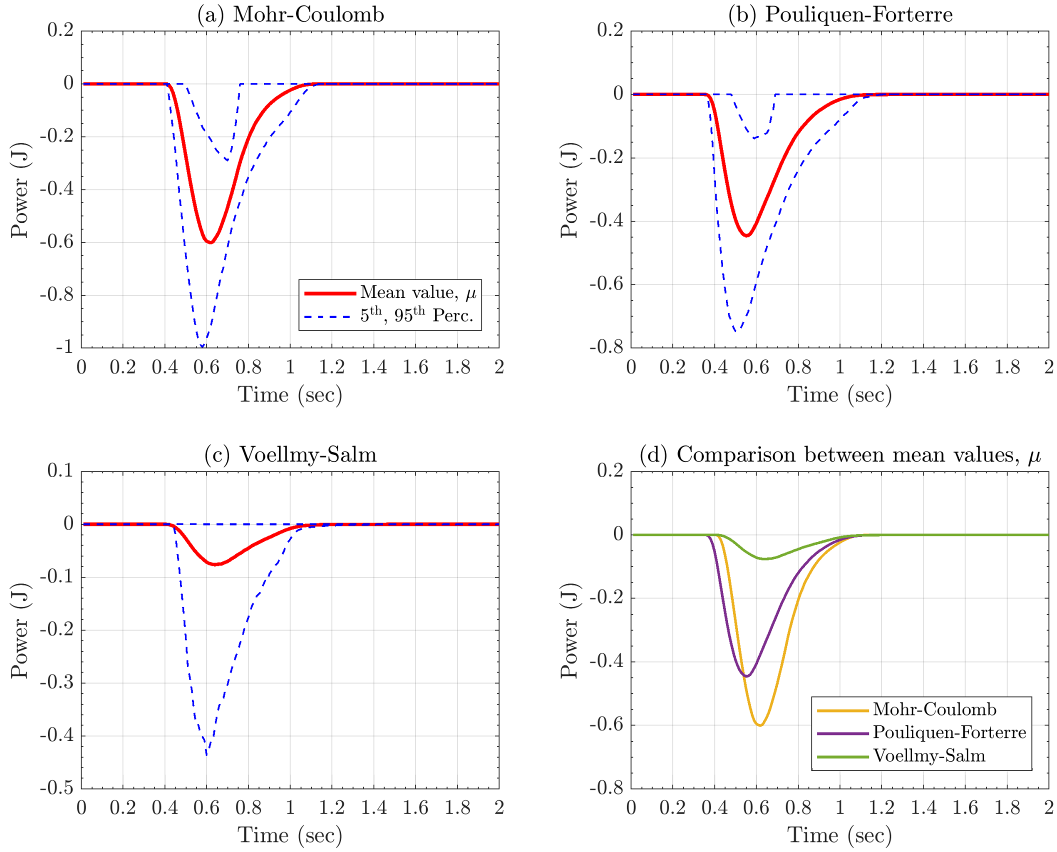

Figure 32: Comparison between mean values of flow acceleration (computed from LHS), $\|\underline{a}\|(L,t)$, recorded at locations of interest, $L_i, \ _{i=1,\ldots,4}$.

- **RHS$_4$**

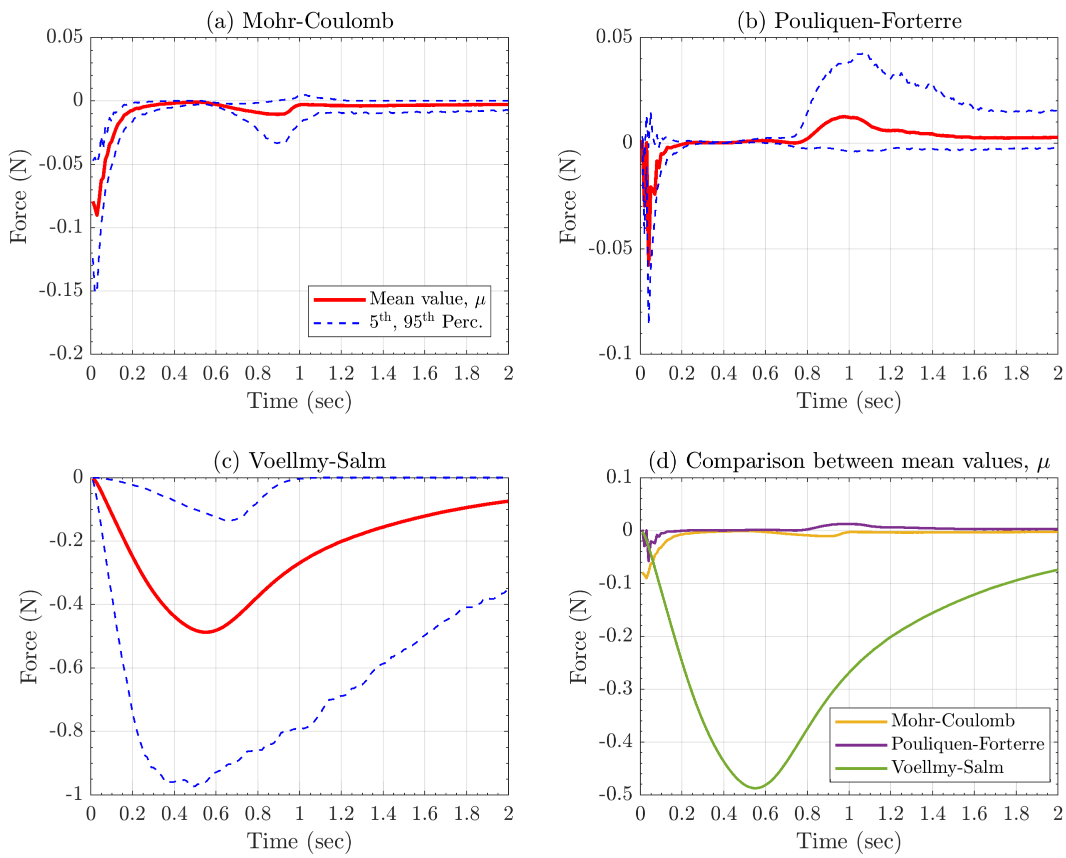

Figure 33: Comparison between mean values of flow acceleration (computed from LHS), $\|\underline{a}\|(L,t)$, recorded at locations of interest, $L_i,\ _{i=1,\dots,4}$.

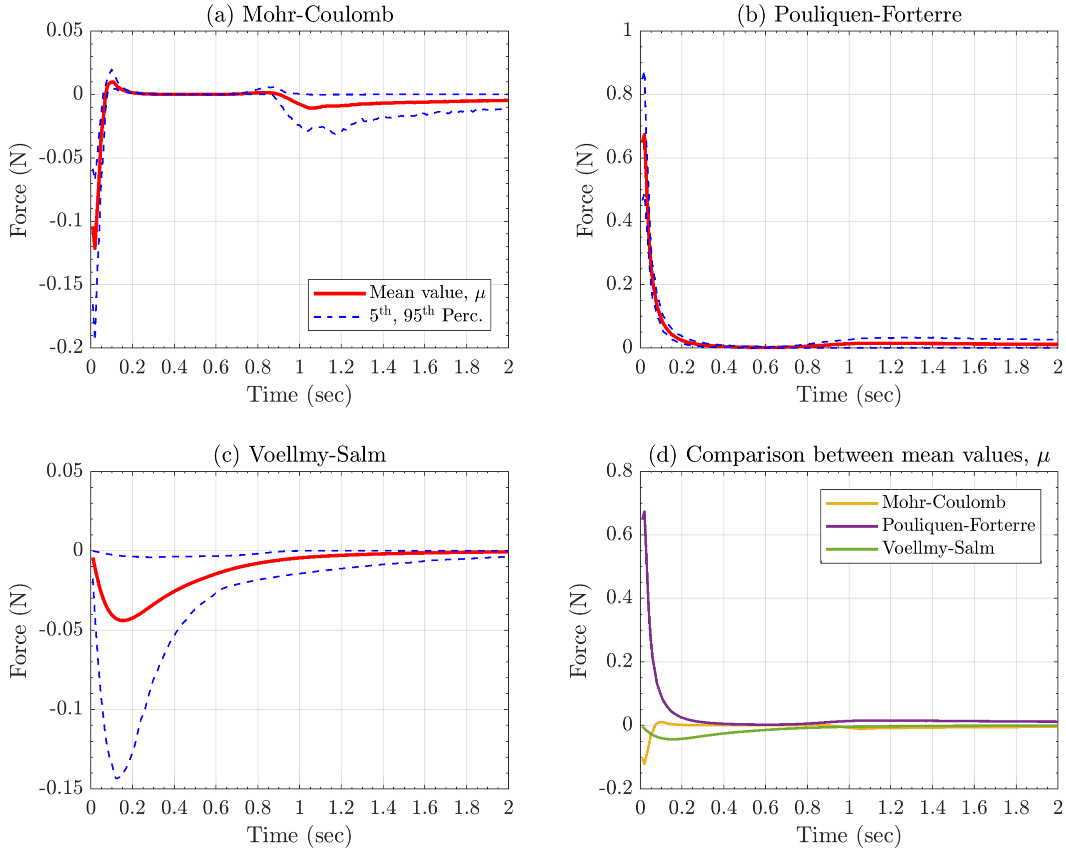

Figure 34: Comparison between mean values of flow acceleration (computed from LHS), $\|\underline{a}\|(L,t)$, recorded at locations of interest, $L_i, \ _{i=1,\dots,4}$.

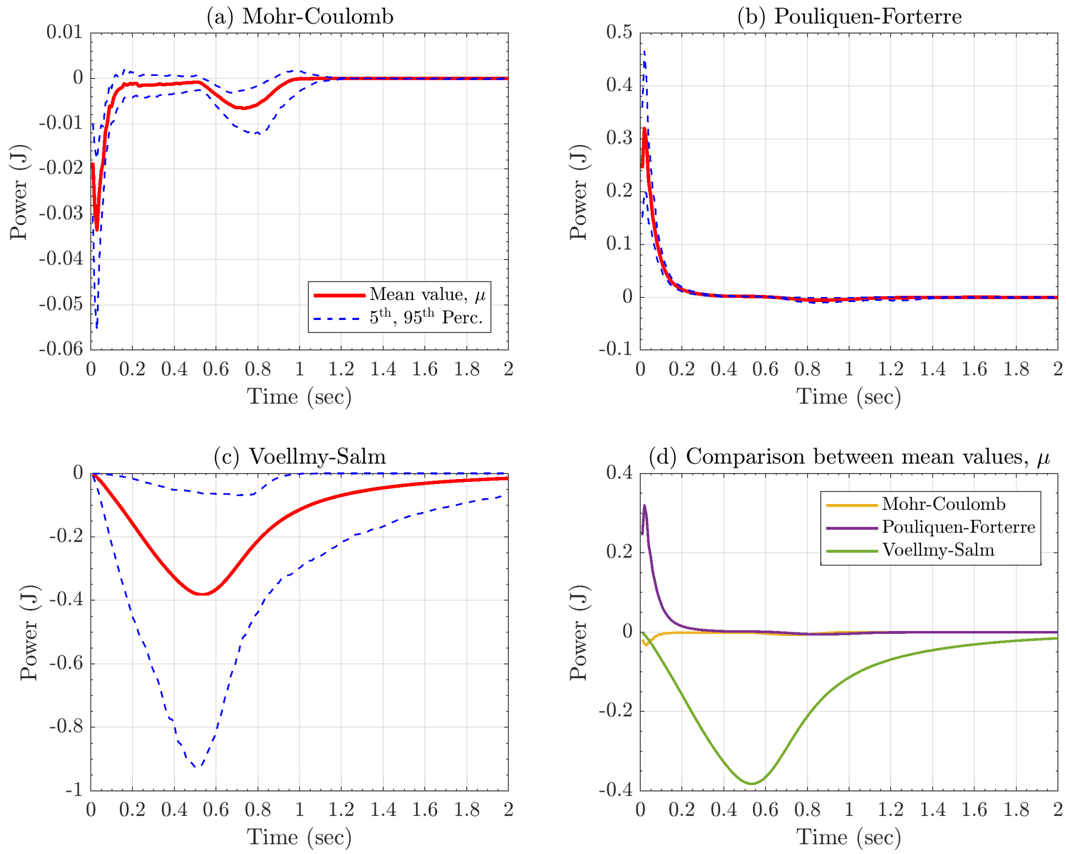

Figure 35: Comparison between mean values of flow acceleration (computed from LHS), $\|\underline{a}\|(L,t)$, recorded at locations of interest, L_i, $_{i=1,\ldots,4}$.

4.1.6 Force contributions - Andrea+Ali

A statistical analysis capable of measuring the contributions of different force components in the rheology models is a fundamental task. This is also necessary to explore and compare the effects of the assumptions behind some modeling choices, onto the time evolution of the flowing material. Let $(F_i(x,t))_{i=1,\ldots,n}$ be the array of force components, where $x \in \mathbb{R}^2$ is a spatial location, and $t \in T$ is a time instant. In our case study, F_1 is the gravitational force, F_2 is the basal friction, F_3 is the curvature correction, F_4 is a resistive force (or the hydrostatic pressure term, in the case of Pouliquen-Forterre rheology). However, this type of procedure can be applied to any additive decomposition of the physical forces. In addition, we can include in the analysis also the component of the inertial forces, i.e. F_4 the convective force and F_5 the transient force. The analysis of local effects can be compared to the contribution of global dynamics.

In this case we are projecting the forces on the directions X and Y, i.e. respectively in the slope direction, and orthogonal to the slope direction on an horizontal plane. Hence in the following the forces are scalar and not vectorial terms. It is important to remark that all the forces are depending on the sample η on the parameter domains, and hence are considered as random variables.

The degree of contribution of those force terms is significantly variable in space and time. For this reason, the following analysis is performed on locally sampled measurements, and not in a spatial averaging framework. In particular, four locations are selected among the center line of the flow. These are: the initial pile location $x_1 = -0.7$ m, the middle of the inclined plane $x_2 = -0.35$ m, the change in slope $x_3 = 0$ m, the middle of the flat plane $x_4 = 0.15$ m. Next notation will assume to be in a selected location $x = x_k$, where $k \in \{1, \dots, 4\}$. The definitions are not depending on the location, but all the results will significantly depend of that choice.

Definition 1 (Contribution coefficients) *Let $(F_i)_{i=1,\dots,n}$ be random variables on $(\Omega, \mathcal{F}, P)$, representing the considered force components in location x at time t. Then, for each component i, the contribution coefficient is defined as:*

$$C_i := \mathbb{E}\left[\frac{F_i}{\Phi}\right],$$

where Φ is a dominating function, i.e. $\Phi \geq |F_i|$, $\forall i$.

The *total force*, i.e $\sum_i F_i$ excluding the inertial terms, is not a good candidate for a dominating function. Indeed, the terms often have opposite signs, and their sum can be really small. Another issue is given by the existence of a subset of times Θ characterized by the absence of flow in the selected location x. In Θ the dominant force is null, and cannot be the denominator of a fraction.

We explore two alternative Φ choices: Φ_1 is based on the l^1 norm, and defined as:

$$\Phi_1 := \begin{cases} \sum_i \frac{|F_i|}{2}, & \text{if not null;} \\ 1, & \text{otherwise.} \end{cases}$$

In case we exclude the inertial forces from the analysis, we must take $\hat{\Phi_1} = 2\Phi_1$. In contrast Φ_2 is the dominant force, based on the l^∞ norm:

$$\Phi_2 := \begin{cases} \max_i |F_i|, & \text{if not null;} \\ 1, & \text{otherwise.} \end{cases}$$

In particular, for a particular location x, time t, and parameter sample η, we have $C_i = 0$ if there is no flow or all the forces are null. The expectation of C_i is reduced by the chance of F_i being small compared to the other terms, or by the chance of having no flow in (x, t). Moreover, $\mathbb{E}[C_i] \in [-1, 1]$, $\forall i$.

Proposition 2 *Let Φ_k, $k = 1, 2$ be the functions described above. Then they are well defined dominating function, i.e. $\Phi_k \geq |F_j|$, $\forall j, k$.*

Proof. If $k = 1$, the Newton equation states $\sum_{j \in J} F_j = \sum_{i \in I} F_i$, where $(F_j)_{j \in J}$ are inertial forces, and $(F_i)_{i \in I}$ the local forces. Then, $\forall h \in I$

$$F_h = \sum_{i \neq h,\ i \in I} F_i - \sum_{j \in J} F_j.$$

And hence

$$|F_h| \leq |F_h| + \sum_{i \neq k,\ i \in I} |F_i| - \sum_{j \in J} |F_j| = 2\Phi_1.$$

A similar equation is valid $\forall k \in J$. If $k = 2$, or if the inertial forces are not included, the proof is trivial. $\square$

Furthermore, assuming $\Phi = \Phi_2$, there is a useful result explaining the meaning of those coefficients through the conditional expectation.

Proposition 3 *Let $(F_i)_{i=1,\dots,n}$ be random variables on $(\Omega, \mathcal{F}, P)$, representing the considered force components in location x at time t. For each i, let C_i be the contribution coefficient of force F_i, assuming $\Phi = \Phi_2$. Then we have the following expression:*

$$C_i = \sum_j p_j \mathbb{E}\left[\frac{F_i}{|F_j|} \;\middle|\; \Phi = |F_j|\right],$$

where $p_j := P\{\Phi = |F_j|\}$.

Proof. Let Z be a discrete random variable such that, for each $j \in \mathbb{N}$, $(Z = j) \iff (\Phi = |F_j|)$. Then, by the rule of chain expectation:

$$C_i = \mathbb{E}\left[\frac{F_i}{\Phi}\right] = \mathbb{E}\left[\mathbb{E}\left[\frac{F_i}{\Phi} \;\middle|\; Z = j\right]\right] =$$

$$= \mathbb{E}\left[\mathbb{E}\left[\frac{F_i}{|F_j|} \;\Big|\; Z=j\right]\right] = \sum_j P\{Z=j\}\, \mathbb{E}\left[\frac{F_i}{|F_j|} \;\Big|\; Z=j\right].$$

Moreover, by definition, $p_j = P\{Z=j\}$. This completes the proof. □

The last proposition brings to the definition of the dominance factors $(p_j)_{j=1,\dots,k}$, i.e. the probability of each F_j to be the dominant force in (x,t).

Definition 4 (Dominance factors and conditional contributions) *Let $(F_i)_{i=1,\dots,k}$ be random variables on $(\Omega, \mathcal{F}, P)$, representing arbitrary force components in location x at time t. Then, for each pair of components (i,j), the conditional contribution $C_{i,j}$ is defined as:*

$$C_{i,j} := \mathbb{E}\left[\frac{F_i}{|F_j|} \;\Big|\; \Phi = |F_j|\right],$$

where $\Phi = \Phi_2$ is the dominant force. In particular, for each component i, the dominance factor is defined as:

$$p_j := P\{\Phi = |F_j|\}.$$

In the following we display the contribution coefficients barplots as a function of time, for the locations $x_1, \dots, x_4$ defined above. Moreover, we report the dominance factors plots, a very useful tool to read the dynamical significance of the forces as a function of time and location.

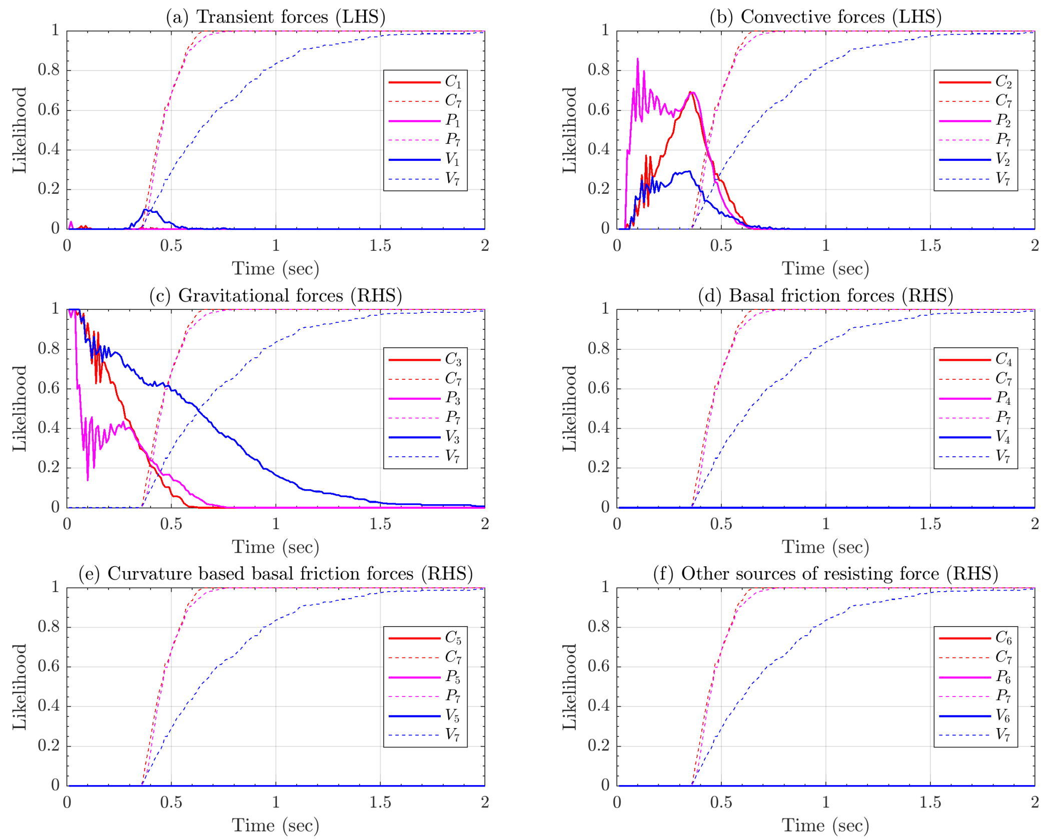

Figure 36: Probability of events $(C_i)_{i=1,\ldots,6} := \{\Phi_2 = |F_i|\}$ for the *Mohr-Coulomb* model, $(P_i)_{i=1,\ldots,6} := \{\Phi_2 = |F_i|\}$ for the *Pouliquen-Forterre* model, $(V_i)_{i=1,\ldots,6} := \{\Phi_2 = |F_i|\}$ for *Voellmy-Salm* model, where F_1 is the *transient force*, F_2 the *convective force*, F_3 the *gravitational force*, F_4 the *basal friction force*, F_5 the *curvature based basal friction force*, and F_6 the *resisting force* (or the hydrostatic pressure term, in the case of Pouliquen-Forterre rheology). Moreover, C_7, P_7, V_7 correspond to the event of *no flow*. All the measurements were recorded at $L_1 = (-0.7, 0)$ and along the runout direction.

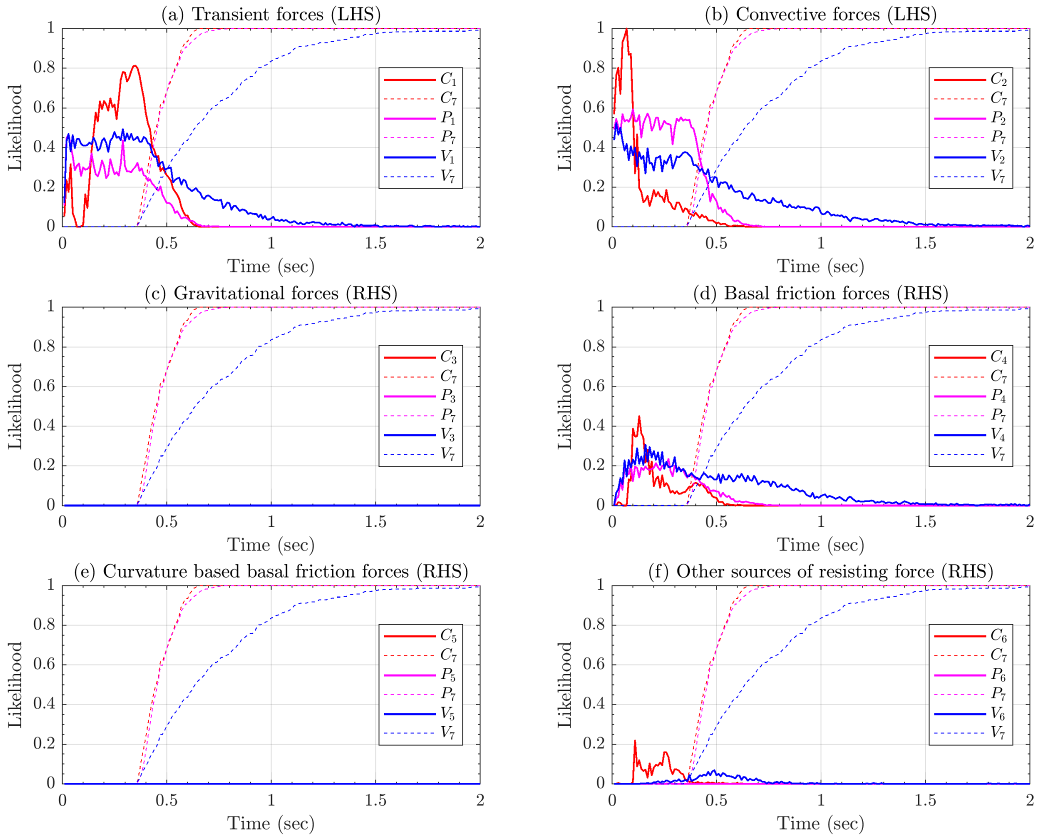

Figure 37: Probability of events $(C_i)_{i=1,\ldots,6} := \{\Phi_2 = |F_i|\}$ for the *Mohr-Coulomb* model, $(P_i)_{i=1,\ldots,6} := \{\Phi_2 = |F_i|\}$ for the *Pouliquen-Forterre* model, $(V_i)_{i=1,\ldots,6} := \{\Phi_2 = |F_i|\}$ for *Voellmy-Salm* model, where F_1 is the *transient force*, F_2 the *convective force*, F_3 the *gravitational force*, F_4 the *basal friction force*, F_5 the *curvature based basal friction force*, and F_6 the *resisting force* (or the hydrostatic pressure term, in the case of Pouliquen-Forterre rheology). Moreover, C_7, P_7, V_7 correspond to the event of *no flow*. All the measurements were recorded at $L_1 = (-0.7, 0)$ and along the lateral direction.

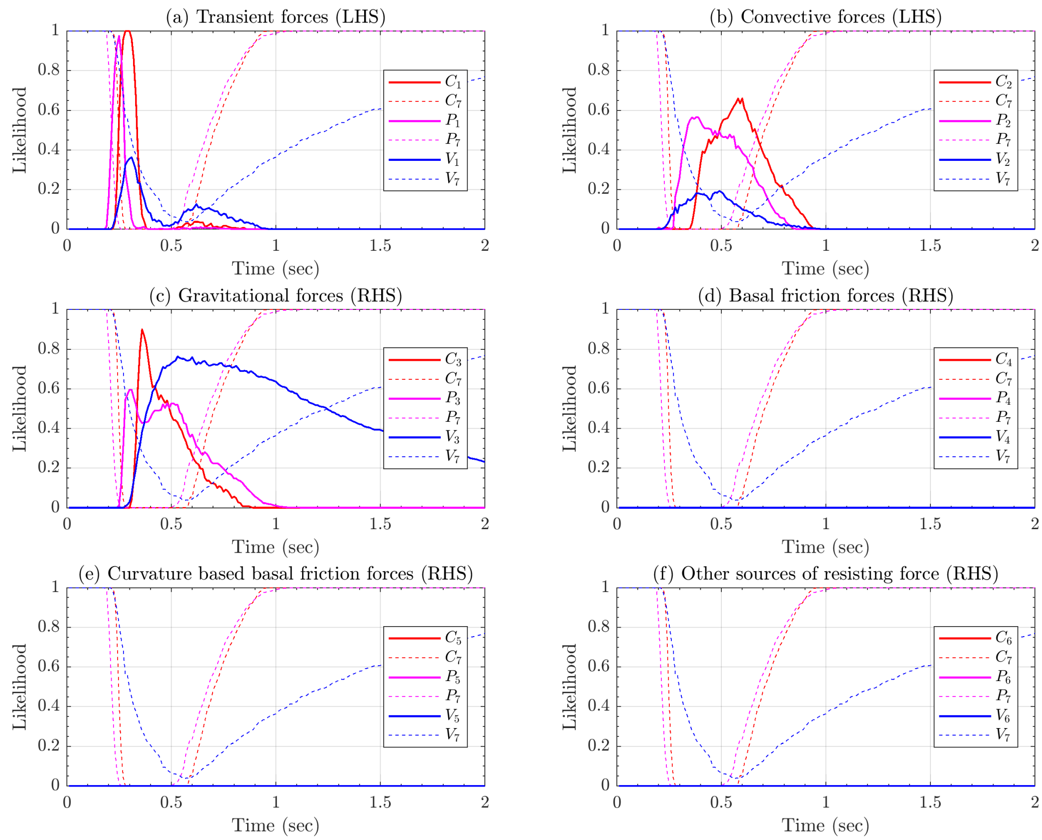

Figure 38: Probability of events $(C_i)_{i=1,\dots,6} := \{\Phi_2 = |F_i|\}$ for the *Mohr-Coulomb* model, $(P_i)_{i=1,\dots,6} := \{\Phi_2 = |F_i|\}$ for the *Pouliquen-Forterre* model, $(V_i)_{i=1,\dots,6} := \{\Phi_2 = |F_i|\}$ for *Voellmy-Salm* model, where F_1 is the *transient force*, F_2 the *convective force*, F_3 the *gravitational force*, F_4 the *basal friction force*, F_5 the *curvature based basal friction force*, and F_6 the *resisting force* (or the hydrostatic pressure term, in the case of Pouliquen-Forterre rheology). Moreover, C_7, P_7, V_7 correspond to the event of *no flow*. All the measurements were recorded at $L_2 = (-0.35, 0)$ and along the runout direction.

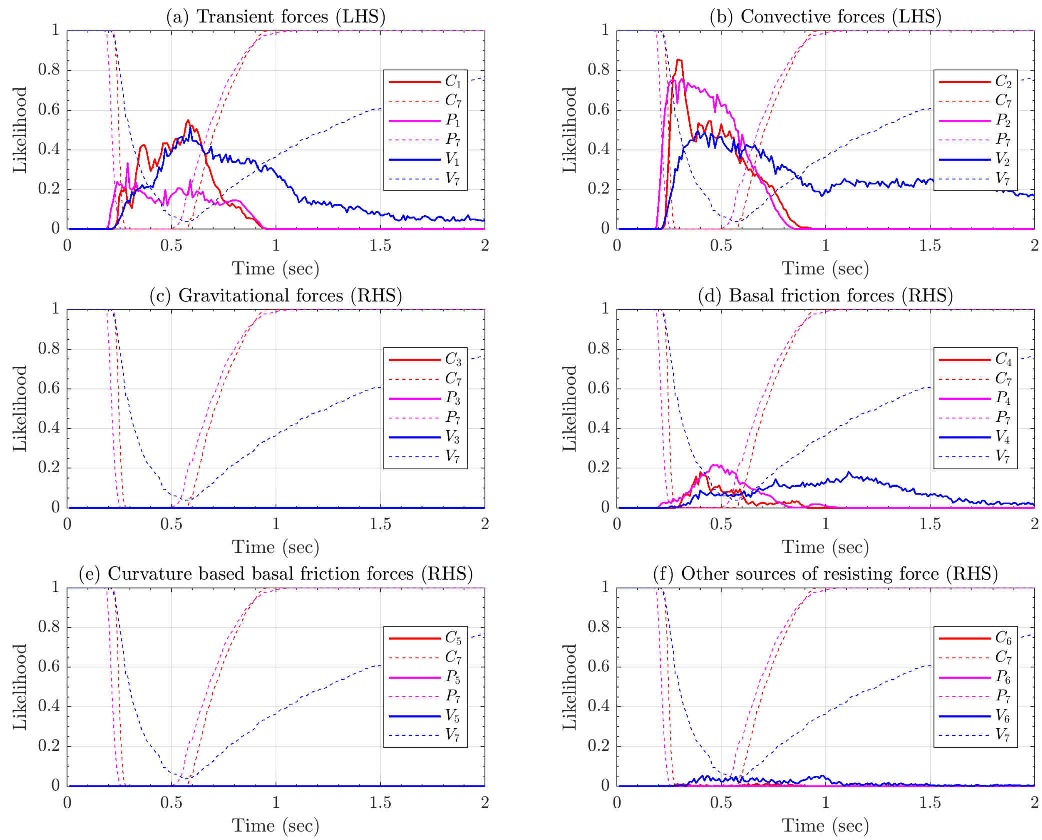

Figure 39: Probability of events $(C_i)_{i=1,\dots,6} := \{\Phi_2 = |F_i|\}$ for the *Mohr-Coulomb* model, $(P_i)_{i=1,\dots,6} := \{\Phi_2 = |F_i|\}$ for the *Pouliquen-Forterre* model, $(V_i)_{i=1,\dots,6} := \{\Phi_2 = |F_i|\}$ for *Voellmy-Salm* model, where F_1 is the *transient force*, F_2 the *convective force*, F_3 the *gravitational force*, F_4 the *basal friction force*, F_5 the *curvature based basal friction force*, and F_6 the *resisting force* (or the hydrostatic pressure term, in the case of Pouliquen-Forterre rheology). Moreover, C_7, P_7, V_7 correspond to the event of *no flow*. All the measurements were recorded at $L_2 = (-0.35, 0)$ and along the lateral direction.

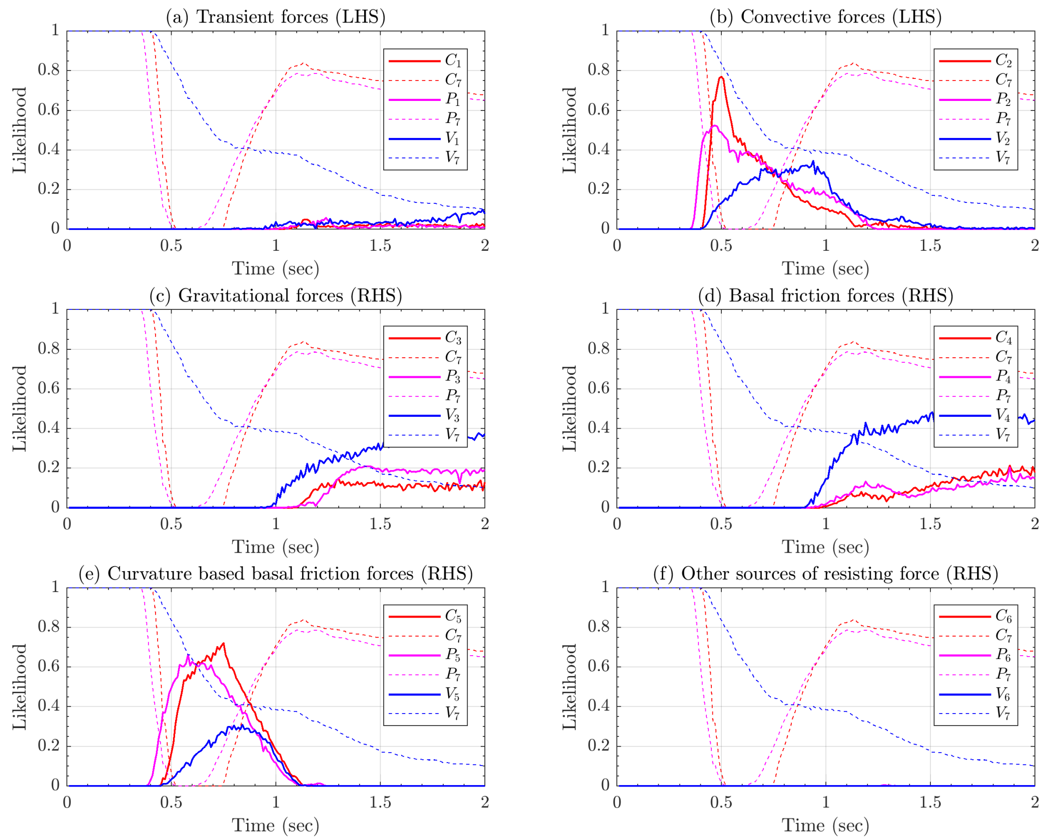

Figure 40: Probability of events $(C_i)_{i=1,\ldots,6} := \{\Phi_2 = |F_i|\}$ for the *Mohr-Coulomb* model, $(P_i)_{i=1,\ldots,6} := \{\Phi_2 = |F_i|\}$ for the *Pouliquen-Forterre* model, $(V_i)_{i=1,\ldots,6} := \{\Phi_2 = |F_i|\}$ for *Voellmy-Salm* model, where F_1 is the *transient force*, F_2 the *convective force*, F_3 the *gravitational force*, F_4 the *basal friction force*, F_5 the *curvature based basal friction force*, and F_6 the *resisting force* (or the hydrostatic pressure term, in the case of Pouliquen-Forterre rheology). Moreover, C_7, P_7, V_7 correspond to the event of *no flow*. All the measurements were recorded at $L_3 = (0, 0)$ and along the runout direction.

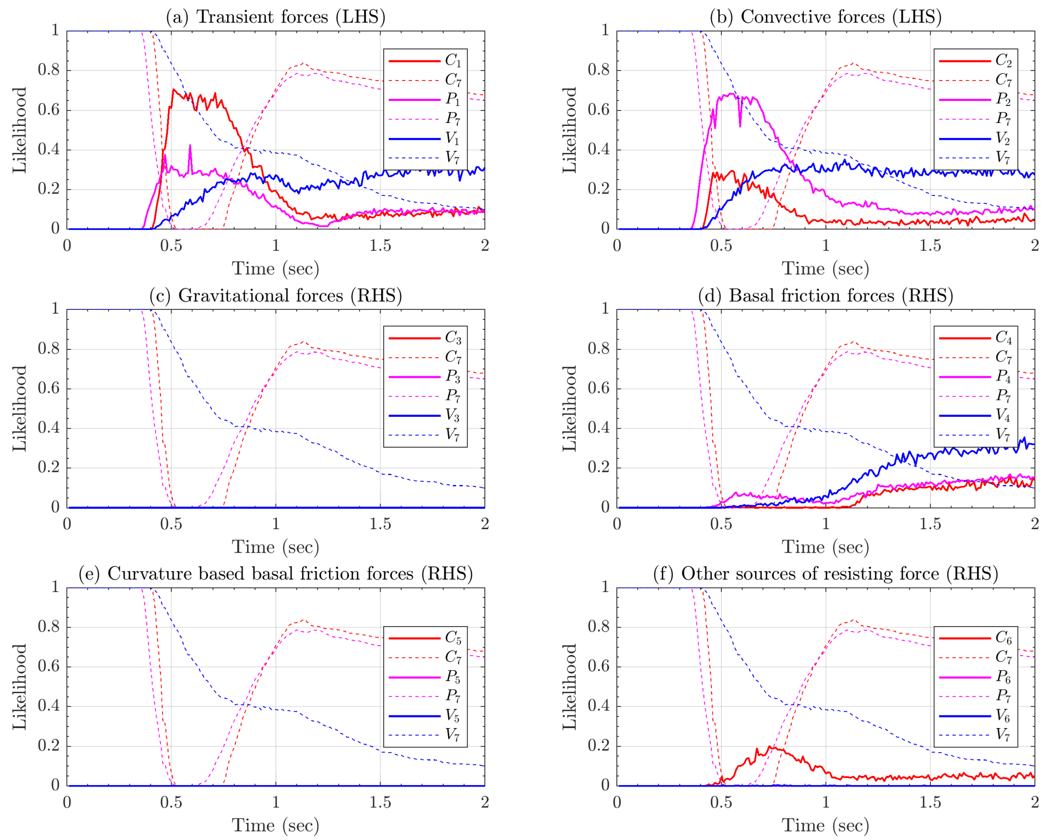

Figure 41: Probability of events $(C_i)_{i=1,\ldots,6} := \{\Phi_2 = |F_i|\}$ for the *Mohr-Coulomb* model, $(P_i)_{i=1,\ldots,6} := \{\Phi_2 = |F_i|\}$ for the *Pouliquen-Forterre* model, $(V_i)_{i=1,\ldots,6} := \{\Phi_2 = |F_i|\}$ for *Voellmy-Salm* model, where F_1 is the *transient force*, F_2 the *convective force*, F_3 the *gravitational force*, F_4 the *basal friction force*, F_5 the *curvature based basal friction force*, and F_6 the *resisting force* (or the hydrostatic pressure term, in the case of Pouliquen-Forterre rheology). Moreover, C_7, P_7, V_7 correspond to the event of *no flow*. All the measurements were recorded at $L_3 = (0, 0)$ and along the lateral direction.

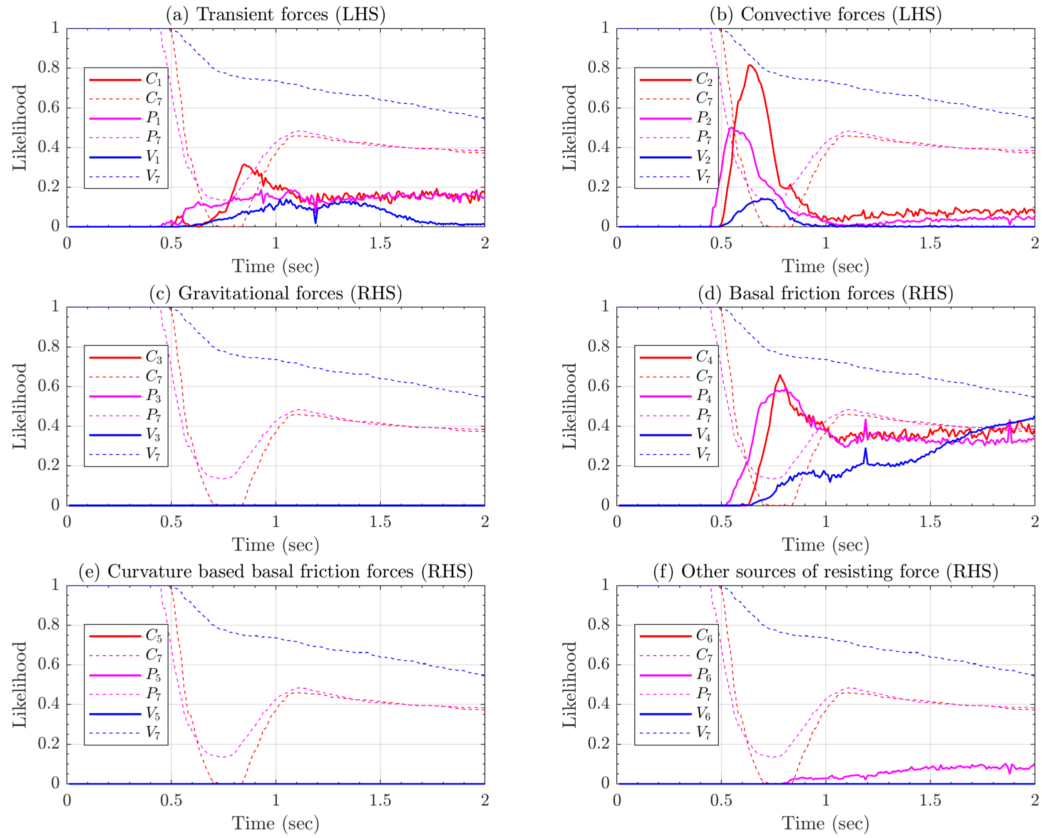

Figure 42: Probability of events $(C_i)_{i=1,\dots,6} := \{\Phi_2 = |F_i|\}$ for the *Mohr-Coulomb* model, $(P_i)_{i=1,\dots,6} := \{\Phi_2 = |F_i|\}$ for the *Pouliquen-Forterre* model, $(V_i)_{i=1,\dots,6} := \{\Phi_2 = |F_i|\}$ for *Voellmy-Salm* model, where F_1 is the *transient force*, F_2 the *convective force*, F_3 the *gravitational force*, F_4 the *basal friction force*, F_5 the *curvature based basal friction force*, and F_6 the *resisting force* (or the hydrostatic pressure term, in the case of Pouliquen-Forterre rheology). Moreover, C_7, P_7, V_7 correspond to the event of *no flow*. All the measurements were recorded at $L_4 = (0.15, 0)$ and along the runout direction.

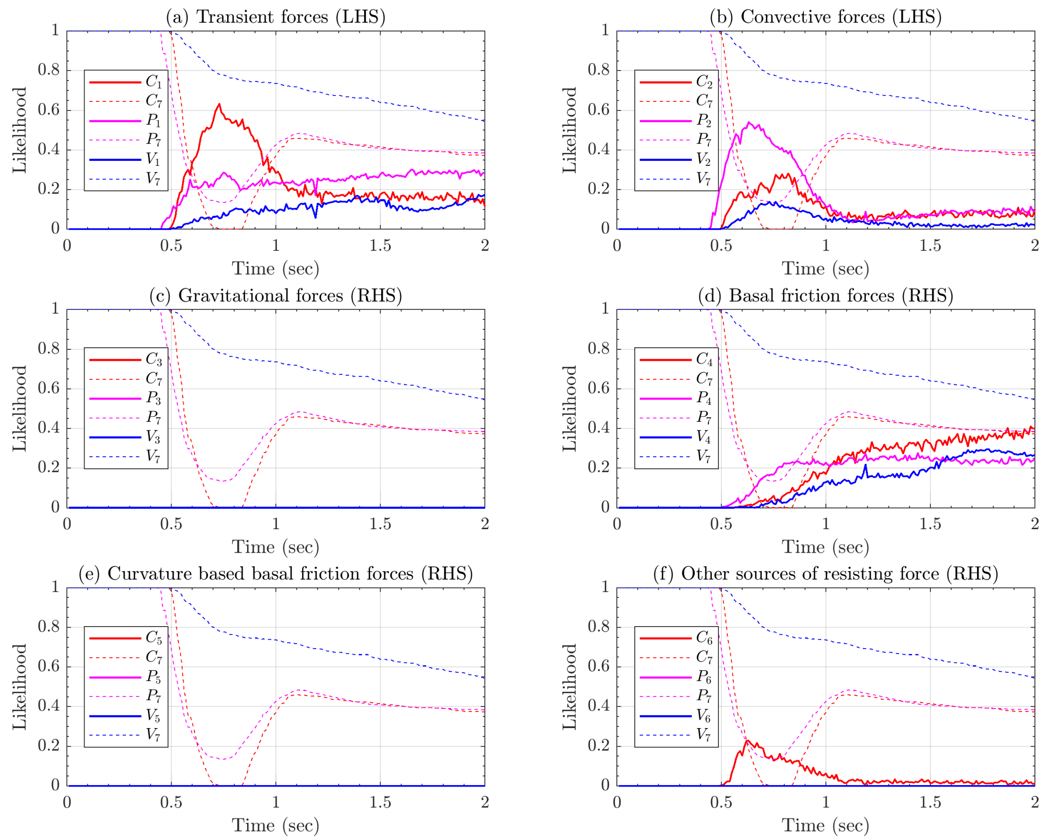

Figure 43: Probability of events $(C_i)_{i=1,\dots,6} := \{\Phi_2 = |F_i|\}$ for the *Mohr-Coulomb* model, $(P_i)_{i=1,\dots,6} := \{\Phi_2 = |F_i|\}$ for the *Pouliquen-Forterre* model, $(V_i)_{i=1,\dots,6} := \{\Phi_2 = |F_i|\}$ for *Voellmy-Salm* model, where F_1 is the *transient force*, F_2 the *convective force*, F_3 the *gravitational force*, F_4 the *basal friction force*, F_5 the *curvature based basal friction force*, and F_6 the *resisting force* (or the hydrostatic pressure term, in the case of Pouliquen-Forterre rheology). Moreover, C_7, P_7, V_7 correspond to the event of *no flow*. All the measurements were recorded at $L_4 = (0.15, 0)$ and along the lateral direction.

5 Results and Discussion – All

Appendix A: Latin Hypercubes and orthogonal arrays - Andrea

The Latin Hypercube Sampling (LHS) is a well established procedure for defining pseudo-random designs of samples in $\mathbb{R}^d$, with good properties with respect to the uniform probability distribution on an hypercube $[0,1]^d$ (McKay et al., 1979; Owen, 1992a; Stein, 1987; Ranjan and Spencer, 2014; Ai et al., 2016). In particular, compared to a random sampling, a LHS: (i) enhances the capability to fill the d-dimensional space with a finite number of points, (ii) in case $d > 1$, avoids the overlapping of point locations in the one dimensional projections, (iii) reduces the dependence of the number of points necessary on the dimensionality d.

Definition 5 (Latin hypercube sampling) *Let $\Xi = \{\xi_i \ : \ i = 1, \dots, N\}$ be a set of points inside the d-dimensional hypercube $C = [0,1]^d$. Let $[0,1] = \bigcup_{j=1}^N I_j$, where $I_j = [\frac{(j-1)}{N}, \frac{j}{N}]$. Let $\xi_i = (\xi_i^1, \dots, \xi_i^d)$,* *and for each $k \in \{1,\dots,d\}$, let $\Xi^k = \{\xi_i^k \ : \ i = 1,\dots,N\}$. Let λ^d be the uniform probability measure supported inside C, called Lebesgue measure. Then Ξ is a latin hypercube w.r.t. $\lambda^d \iff \forall j \in \{1,\dots,N\}$, $\forall k \in \{1,\dots,d\}$, $\left|I_j \cap \Xi^k\right| = 1$.*

The procedure is simple: once the desired number of samples $N \in \mathbb{N}$ is selected, and $[0,1]$ is divided in N equal bins, then each bin will contain one and only one projection of the samples over every coordinate. The LHS definition is trivially generalized over $C = \prod_i^d [a_i, b_i]$, i.e. the cartesian product of d arbitrary intervals. That will be applied in this study, defining LHS over the parameter domain of the flow models.

There are a large number of possible designs, corresponding the number of permutations of the bins in the d-projections, i.e. $d \cdot N!$. If the permutations are randomly sampled there is a high possibility that the design will have good properties. However, this is not assured, and clusters o points or regions of void space may be observed in C. For this reason, we base our design on the orthogonal arrays (OA) (Owen, 1992b; Tang, 1993).

Definition 6 (Orthogonal arrays) *Let $S = \{1,\dots,s\}$, where $s \geq 2$. Let $Q \in S^{n\times m}$ be a matrix of such integer values. Then Q is called an $OA(n,m,s,r) \iff$ each $n \times r$ submatrix of Q contains all possible $1 \times r$ row vectors with the same frequency $\lambda = n/s^r$, which is called the index of the array. In particular, r is called the strength, n the size, $(m \geq r)$ the constrains, and s the levels of the array.*

Orthogonal arrays are very useful for defining latin hypercubes which are also forced to fill the space (or its r-dimensional subspaces) in a more robust way, at the cost of potentially requiring a larger number of points than a traditional LHS.

Proposition 7 *Let Q be an $OA(n,m,s,r)$. Then let $U \in \mathbb{R}^{n\times m}$ be defined as follows:*

$$\forall k \in \{1,\dots,s\},\ \forall j \in \{1,\dots,m\},\ \{Q[\cdot,j] \ : \ Q[i,j] = k\} = \Pi\left(\{(k-1)\lambda s^{r-1},\dots,k\lambda s^{r-1}\}\right),$$

where Π is a random permutation of λs^{r-1} elements. Then $\Xi = \{\xi_i = U[i,\cdot] \ : \ i = 1,\dots,n\}$ is a LHS w.r.t to λ^m over $C = [0,1]^m$. Moreover, let $[0,1]^r = \bigcup_{(h_1,\dots,h_r)=1}^s I_{(h_i)}$, where $I_{(h_i)} = \prod_i^r [\frac{(h_i-1)}{s}, \frac{h_i}{s}]$. Then $\forall D = (d_1,\dots,d_r) \subseteq \{1,\dots,m\}$, let $\Xi^D = \{(\xi^{d_1},\dots,\xi^{d_r}) \ : \ i = 1,\dots,n\}$. We have that

$$\forall k \in \{1,\dots,s\},\ \forall (h_i \ : i = 1,\dots,r) \in \{1,\dots,d\}^r,\ \left|I_{(k_i)} \cap \Xi^D\right| = \lambda.$$

For each column of Q we are replacing the λs^{r-1} elements with entry k by a random permutation of $\left((k-1)\lambda s^{r-1} + h\right)_{h\in 1,\dots,\lambda s^{r-1}}$. After the replacement procedure is done, the newly obtained matrix U is equivalent to a LHS which inherits from Q the property of fully covering s^r equal r-dimensional hypercubes in every r-dimensional projection. Each hypercube contains λ points. In other words, inside each r-dimensional projection, the design associated to U fills the space like a regular grid at the scale of those s^r hypercubes, but it is still an LHS at a finer scale, i.e. the λs^{r-1} one dimensional bins. A complete proof can be found in Tang (1993) and it is a straightforward verification of the required properties.

However, even in an LHS based on an $OA(n,m,s,r)$, if $r < m$ what happens in the projections with dimension $r' > r$ is not controlled, and randomizing procedures are made more difficult by the additional structure imposed by the OA. Moreover, the total number of points necessary to achieve a full design increases with r, and hence is affected by dimensionality issues.

Dealing with relatively small d, i.e. $d \in \{3,4\}$, we adopt a LHS U created by a $OA(s^d,d,s,d)$. The strength is equal to the dimension d, hence the design fills the entire space like a d dimensional grid, but it is a LHS as well. In this case there is one point in each hypercube, and $\lambda = 1$. We take $s = 8$ for the 3-dimensional designs over the parameter space of Mohr-Coulomb and Voellmy-Salm models, i.e. 512 points; we took $s = 6$ for the 4-dimensional designs over the more complex parameter space of the Pouliquen-Forterre model, i.e. 1296 points.

References

Aghakhani, H., Dalbey, K., Salac, D., and Patra, A. K. (2016). Heuristic and Eulerian interface capturing approaches for shallow water type flow and application to granular flows. *Computer Methods in Applied Mechanics and Engineering*, 304:243–264.

Ai, M., Kong, X., and Li, K. (2016). A general theory for orthogonal array based latin hypercube sampling. *Statistica Sinica*, (26):761–777.

Balmforth, N. J. and Kerswell, R. R. (2005). Granular collapse in two dimensions. *Journal of Fluid Mechanics*, 538:399–428.

Barker, T., Schaeffer, D. G., Bohorquez, P., and Gray, J. M. N. T. (2015). Well-posed and ill-posed behaviour of the $\mu(i)$ -rheology for granular flow. *Journal of Fluid Mechanics*, 779:794—818.

Bartelt, P. and McArdell, B. (2009). Granulometric investigations of snow avalanches. *Journal of Glaciology*, 55(193):829–833(5).

Bartelt, P., Salm, B., and Gruber, U. (1999). Calculating dense-snow avalanche runout using a voellmy-fluid model with active/passive longitudinal straining. *Journal of Glaciology*, 45(150):242–254.

Batchelor, G. (2000). *An Introduction to Fluid Dynamics.* Cambridge Mathematical Libraries. Cambridge University Press.

Bayarri, M. J., Berger, J. O., Calder, E. S., Dalbey, K., Lunagomez, S., Patra, A. K., Pitman, E. B., Spiller, E. T., and Wolpert, R. L. (2009). Using Statistical and Computer Models to Quantify Volcanic Hazards. *Technometrics*, 51(4):402–413.

Bayarri, M. J., Berger, J. O., Calder, E. S., P. A. K. P. E. B., Spiller, E. T., and Wolpert, R. L. (2015). Probabilistic Quantification of Hazards: A Methodology Using Small Ensembles of Physics-Based Simulations and Statistical Surrogates. *International Journal for Uncertainty Quantification*, 5(4):297–325.

Bursik, M., Patra, A., Pitman, E. B., Nichita, C., Macias, J. L., Saucedo, R., and Girina, O. (2005). Advances in studies of dense volcanic granular flows. *Reports on Progress in Physics*, 68(2):271.

Capra, L., Gavilanes-Ruiz, J. C., Bonasia, R., Saucedo-Giron, R., and Sulpizio, R. (2015). Re-assessing volcanic hazard zonation of volcán de colima, méxico. *Natural Hazards*, 76(1):41–61.

Capra, L., Macís, J., Cortés, A., Dávila, N., Saucedo, R., Osorio-Ocampo, S., Arce, J., Gavilanes-Ruiz, J., Corona-Chávez, P., García-Sánchez, L., Sosa-Ceballos, G., and Vázquez, R. (2016). Preliminary report on the july 10–11, 2015 eruption at volcán de colima: Pyroclastic density currents with exceptional runouts and volume. *Journal of Volcanology and Geothermal Research*, 310(Supplement C):39 – 49.

Capra, L., Manea, V. C., Manea, M., and Norini, G. (2011). The importance of digital elevation model resolution on granular flow simulations: a test case for colima volcano using titan2d computational routine. *Natural Hazards*, 59(2):665–680.

Charbonnier, S., Germa, A., Connor, C., Gertisser, R., Preece, K., Komorowski, J.-C., Lavigne, F., Dixon, T., and Connor, L. (2013). Evaluation of the impact of the 2010 pyroclastic density currents at merapi volcano from high-resolution satellite imagery, field investigations and numerical simulations. *Journal of Volcanology and Geothermal Research*, 261(Supplement C):295 – 315. Merapi eruption.

Charbonnier, S. J. and Gertisser, R. (2009). Numerical simulations of block-and-ash flows using the titan2d flow model: examples from the 2006 eruption of merapi volcano, java, indonesia. *Bulletin of Volcanology*, 71(8):953–959.

Christen, M., Kowalski, J., and Bartelt, P. (2010). RAMMS: Numerical simulation of dense snow avalanches in three-dimensional terrain. *Cold Regions Science and Technology*, 63:1–14.

DaCruz, F., Emam, S., Prochnow, M., Roux, J.-N., and Chevoir, F. (2005). Rheophysics of dense granular materials: Discrete simulation of plane shear flows. *Physical Review E*, 72:021309.

Dade, W. B. and Huppert, H. E. (1998). Long-runout rockfalls. *Geology*, 26(9):803–806.

Dalbey, K., Patra, A. K., Pitman, E. B., Bursik, M. I., and Sheridan, M. F. (2008). Input uncertainty propagation methods and hazard mapping of geophysical mass flows. *Journal of Geophysical Research: Solid Earth*, 113:1–16.

Dalbey, K. R. (2009). *Predictive Simulation and Model Based Hazard Maps*. PhD thesis, University at Buffalo.

Davila, N., Capra, L., Gavilanes-Ruiz, J., Varley, N., Norini, G., and Vazquez, A. G. (2007). Recent lahars at volcán de colima (mexico): Drainage variation and spectral classification. *Journal of Volcanology and Geothermal Research*, 165(3):127 – 141.

Denlinger, R. P. and Iverson, R. M. (2001). Flow of variably fluidized granular masses across three-dimensional terrain: 2. Numerical predictions and experimental tests. *Journal of Geophysical Research*, 106(B1):553–566.

Denlinger, R. P. and Iverson, R. M. (2004). Granular avalanches across irregular three-dimensional terrain: 1. Theory and computation. *Journal of Geophysical Research (Earth Surface)*, 109(F1):F01014.

Edwards, A. N. and Gray, J. M. N. T. (2015). Erosion-deposition waves in shallow granular free-surface flows. *Journal of Fluid Mechanics*, 762:35–67.

Fischer, J., Kowalski, J., and Pudasaini, S. P. (2012). Topographic curvature effects in applied avalanche modeling. *Cold Regions Science and Technology*, 74-75:21–30.

Forterre, Y. (2006). Kapiza waves as a test for three-dimensional granular flow rheology. 563(Journal of Fluid Mechanics):123–132.

Forterre, Y. and Pouliquen, O. (2002). Stability analysis of rapid granular chute flows: formation of longitudinal vortices. *Journal of Fluid Mechanics*, 467:361–387.

Forterre, Y. and Pouliquen, O. (2003). Long-surface-wave instability in dense granular flows. *Journal of Fluid Mechanics*, 486:21–50.

Fraccarollo, L. and Toro, E. F. (1995). Experimental and numerical assessment of the shallow water model for two dimensional dam-break type problems. *Journal of Hydraulic Research*, 33:843–864.

Freundt, A. and Bursik, M. I. (1998). Pyroclastic flow transport mechanisms. In Freundt, A. and Rosi, M., editors, *From Magma to Tephra: Modelling Physical Processes of Explosive Volcanism*, volume 4 of *Advances in Volcanology*, pages 151–222. Elsevier Science, Amsterdam.

González, M. B., Ramírez, J. J., and Navarro, C. (2002). Summary of the historical eruptive activity of volcán de colima, mexico 1519–2000. *Journal of Volcanology and Geothermal Research*, 117(1):21 – 46.

Gray, J. M. N. T. and Edwards, A. N. (2014). A depth-averaged $\mu(I)$-rheology for shallow granular free-surface flows. *Journal of Fluid Mechanics*, 755:503–534.

Gray, J. M. N. T., Tai, Y. C., and Noelle, S. (2003). Shock waves, dead zones and particle-free regions in rapid granular free-surface flows. *Journal of Fluid Mechanics*, 491:161–181.

Gray, J. M. N. T., Wieland, M., and Hutter, K. (1999). Gravity-driven free surface flow of granular avalanches over complex basal topography. *Proceedings of the Royal Society A: Mathematical, Physical and Engineering Sciences*, 455(1985):1841–1874.

Greve, R., Koch, T., and Hutter, K. (1994). Unconfined flow of granular avalanches along a partly curved surface: experiments and theoretical predictions. *Proc. R. Soc. London Ser. A*, 342:573–600.

Gruber, U. and Bartelt, P. (2007). Snow avalanche hazard modelling of large areas using shallow water numerical models and GIS. *Environmrntal Modelling & Software*, 22:1472–1481.

Hutter, K., Siegel, M., Savage, S. B., and Nohguchi, Y. (1993). Two-dimensional spreading of a granular avalanche down an inclined plane part I. Theory. *Acta Mechanica*, 100:37–68.

Iordanoff, I. P. and Khonsari, M. M. (2004). Granular Lubrication: Toward an Understanding of the Transition Between Kinetic and Quasi-Fluid Regime. *Journal of Tribology*, 126(1):137–145.

Iverson, R. M. (1997). The physics of debris flows. *Reviews of Geophysics*, 35:245–296.

Iverson, R. M. and Denlinger, R. P. (2001). Flow of variably fluidized granular masses across three-dimensional terrain: 1. Coulomb mixture theory. *Journal of Geophysical Research*, 106(B1):537.

Iverson, R. M. and George, D. L. (2014). A depth-averaged debris-flow model that includes the effects of evolving dilatancy. i. physical basis. *Proceedings of the Royal Society of London A: Mathematical, Physical and Engineering Sciences*, 470(2170).

Iverson, R. M., Logan, M., and Denlinger, R. P. (2004). Granular avalanches across irregular three-dimensional terrain: 2. experimental tests. *Journal of Geophysical Research: Earth Surface*, 109(F1):n/a–n/a. F01015.

Jaeger, H. M., Liu, C., and Nagel, S. R. (1989). Relaxation at the Angle of Repose. *Physical Reviiew Letters*, 62(1):40–43.

Jop, P., Forterre, Y., and Pouliquen, O. (2006). A constitutive law for dense granular flows. *Nature*, 441:727–730.

Kelfoun, K. (2011). Suitability of simple rheological laws for the numerical simulation of dense pyroclastic flows and long-runout volcanic avalanches. *Journal of Geophysical Research*, 116:B08209.

Kelfoun, K. and Druitt, T. H. (2005). Numerical modeling of the emplacement of socompa rock avalanche, chile. *Journal of Geophysical Research: Solid Earth*, 110(B12).

Kelfoun, K., Samaniego, P., Palacios, P., and Barba, D. (2009). Testing the suitability of frictional behaviour for pyroclastic flow simulation by comparison with a well-constrained eruption at Tungurahua volcano (Ecuador). *Bulletin of Volcanology*, 71:1057–1075.

Kern, M., Bartelt, P., Sovilla, B., and Buser, O. (2009). Measured shear rates in large dry and wet snow avalanches. *Journal of Glaciology*, 55(190):327–338.

la Cruz-Reyna, S. D. (1993). Random patterns of occurrence of explosive eruptions at colima volcano, mexico. *Journal of Volcanology and Geothermal Research*, 55(1):51 – 68.

Lajeunesse, E., Monnier, J. B., and Homsy, G. M. (2005). Granular slumping on a horizontal surface. *Phys. Fluids*, 17:103302.

Luca, I., Tai, Y., and Kuo, C. (2016). *Shallow Geophysical Mass Flows down Arbitrary Topography: Model Equations in Topography-fitted Coordinates, Numerical Simulation and Back-calculations of Disastrous Events*. Advances in Geophysical and Environmental Mechanics and Mathematics. Springer International Publishing.

Mangeney-Castelnau, A., Bouchut, F., Thomas, N., Vilotte, J. P., and Bristeau, M.-O. (2007). Numerical modeling of self-channeling granular flows and of their levee/channel deposits. *J. Geophys. Res.*, 112:F02017.

Mangeney-Castelnau, A., Bouchut, F., Vilotte, J. P., Lajeunesse, E., Aubertin, A., and Pirulli, M. (2005). On the use of Saint-Venant equations to simulate the spreading of a granular mass. *J. Geophys. Res.*, 110:B09103.

Martin Del Pozzo, A. M., Sheridan, M. F., Barrera, M., Hubp, J. L., and Selem, L. V. (1995). Potential hazards from Colima Volcano, Mexico. *Geofisica Internacional*, 34:363–376.

McKay, M. D., Beckman, R. J., and Conover, W. J. (1979). A comparison of three methods for selecting values of input variables in the analysis of output from a computer code. *Technometrics*, 21(2):239–245.

Norini, G., De Beni, E., Andronico, D., Polacci, M., Burton, M., and Zucca, F. (2009). The 16 november 2006 flank collapse of the south-east crater at mount etna, italy: Study of the deposit and hazard assessment. *Journal of Geophysical Research: Solid Earth*, 114(B2):n/a–n/a. B02204.

Ogburn, S. E., Berger, J., Calder, E. S., Lopes, D., Patra, A., Pitman, E. B., Rutarindwa, R., Spiller, E., , and Wolpert, R. L.

Owen, A. B. (1992a). A Central Limit Theorem for Latin Hypercube Sampling. *Journal of the Royal Statistical Society.*, 54(2):541–551.

Owen, A. B. (1992b). Orthogonal arrays for computer experiments, integration and visualization. *Statistica Sinica*, 2(2):439–452.

Patra, A., Nichita, C., Bauer, A., Pitman, E., Bursik, M., and Sheridan, M. (2006). Parallel adaptive discontinuous galerkin approximation for thin layer avalanche modeling. *Computers & Geosciences*, 32(7):912 – 926. Computer Simulation of natural phenomena for Hazard Assessment.

Patra, A. K., Bauer, A. C., Nichita, C. C., Pitman, E. B., Sheridan, M. F., Bursik, M., Rupp, B., Webber, A., Stinton, A. J., Namikawa, L. M., and Renschler, C. S. (2005). Parallel adaptive numerical simulation of dry avalanches over natural terrain. *Journal of Volcanology and Geothermal Research*, 139(1-2):1–21.

Pirulli, M., Bristeau, M. O., Mangeney, A., and Scavia, C. (2007). The effect of the earth pressure coefficients on the runout of granular material. *Environmental Modelling & Software*, 22(10):1437–1454.

Pirulli, M. and Mangeney, A. (2008). Results of Back–Analysis of the Propagation of Rock Avalanches as a Function of the Assumed Rheology. *Rock Mechanics and Rock Engineering*, 41(1):59–84.

Pitman, E., Nichita, C., Patra, A., Bauer, A., Bursik, M., and Webb, A. (2003a). A model of granular flows over an erodible surface. *Discrete and Continuous Dynamical Systems - Series B*, 3(4):589–599.

Pitman, E. B. and Le, L. (2005). A two-fluid model for avalanche and debris flows. *Philosophical transactions. Series A, Mathematical, physical, and engineering sciences*, 363(1832):1573–601.

Pitman, E. B., Nichita, C. C., Patra, A., Bauer, A., Sheridan, M., and Bursik, M. (2003b). Computing granular avalanches and landslides. *Physics of Fluids*, 15(12):3638.

Pouliquen, O. (1999). Scaling laws in granular flows down rough inclined planes. *Physics of Fluids*, 11(3):542–548.

Pouliquen, O. and Forterre, Y. (2002). Friction law for dense granular flows: application to the motion of a mass down a rough inclined plane. *Journal of Fluid Mechanics*, 453:133–151.

Procter, J. N., Cronin, S. J., Platz, T., Patra, A., Dalbey, K., Sheridan, M., and Neall, V. (2010). Mapping block-and-ash flow hazards based on titan 2d simulations: a case study from mt. taranaki, nz. *Natural Hazards*, 53(3):483–501.

Pudasaini, S. and Hutter, K. (2007). *Avalanche Dynamics: Dynamics of Rapid Flows of Dense Granular Avalanches*. Springer.

Pudasaini, S. P. and Hutter, K. (2003). Rapid shear flows of dry granular masses down curved and twisted channels. *Journal of Fluid Mechanics*, 495:193–208.

Ranjan, P. and Spencer, N. (2014). Space-filling latin hypercube designs based on randomization restrictions in factorial experiments. *Statistics and Probability Letters*, 94(Supplement C):239 – 247.

Reyes-Dvila, G. A., Armbula-Mendoza, R., Espinasa-Perea, R., Pankhurst, M. J., Navarro-Ochoa, C., Savov, I., Vargas-Bracamontes, D. M., Corts-Corts, A., Gutirrez-Martnez, C., Valds-Gonzlez, C., Domnguez-Reyes, T., Gonzlez-Amezcua, M., Martnez-Fierros, A., Ramrez-Vzquez, C. A., Crdenas-Gonzlez, L., Castaeda-Bastida, E., de los Monteros, D. M. V. E., Nieto-Torres, A., Campion, R., Courtois, L., and Lee, P. D. (2016). Volcan de colima dome collapse of july, 2015 and associated pyroclastic density currents. *Journal of Volcanology and Geothermal Research*, 320(Supplement C):100 – 106.

Rupp, B. (2004). An analysis of granular flows over natural terrain. Master's thesis, University at Buffalo.

Rupp, B., Bursik, M., Namikawa, L., Webb, A., Patra, A. K., Saucedo, R., Macías, J. L., and Renschler, C. (2006). Computational modeling of the 1991 block and ash fows at Colima Volcano, Mèxico. *Geological Society of America Special Papers*, 402(11):223–237.

Ruyer-Quil, C. and Manneville, P. (2000). Improved modeling of flows down inclined planes. *Eur. Phys. J. B*, 15:357–369.

Salm, B. (1993). Flow, flow transition and runout distances of flowing avalanches. *Annals of Glaciology*, 18:221–226.

Salm, B., Burkard, A., and Gubler, H. (1990). Berechnung von Fliesslawinen: eine Anleitung für Praktiker mit Beispielen. *Mitteilungen des Eidgenössische Institutes für Schnee- und Lawinenforschung*, 47.

Sarocchi, D., Sulpizio, R., Macías, J., and Saucedo, R. (2011). The 17 july 1999 block-and-ash flow (baf) at colima volcano: New insights on volcanic granular flows from textural analysis. *Journal of Volcanology and Geothermal Research*, 204(1):40 – 56.

Saucedo, R., Macías, J., Bursik, M., Mora, J., Gavilanes, J., and Cortes, A. (2002). Emplacement of pyroclastic flows during the 1998–1999 eruption of volcán de colima, méxico. *Journal of Volcanology and Geothermal Research*, 117(1):129 – 153.

Saucedo, R., Macías, J., Gavilanes, J., Arce, J., Komorowski, J., Gardner, J., and Valdez-Moreno, G. (2010). Eyewitness, stratigraphy, chemistry, and eruptive dynamics of the 1913 plinian eruption of volcán de colima, méxico. *Journal of Volcanology and Geothermal Research*, 191(3–4):149 – 166.

Saucedo, R., Macías, J., Sheridan, M., Bursik, M., and Komorowski, J. (2005). Modeling of pyroclastic flows of colima volcano, mexico: implications for hazard assessment. *Journal of Volcanology and Geothermal Research*, 139(1):103 – 115. Modeling and Simulation of Geophysical Mass Flows.

Saucedo, R., Macías, J. L., and Bursik, M. (2004). Pyroclastic flow deposits of the 1991 eruption of Volcán de Colima, Mexico. *Bulletin of Volcanology*, 66(4):291–306.

Savage, S. B. and Hutter, K. (1989). The motion of a finite mass of granular material down a rough incline. *Journal of Fluid Mechanics*, 199:177.

Savage, S. B. and Iverson, R. M. (2003). Surge dynamics coupled to pore-pressure evolution in debris flows. *Debris-Flow Hazards Mitigation: Mechanics, Prediction and Assessment, edited by: Rickenmann, D. and Chen, C. L., Millpress*, 1:503–514.

Sheridan, M., Stinton, A., Patra, A., Pitman, E., Bauer, A., and Nichita, C. (2005). Evaluating titan2d mass-flow model using the 1963 little tahoma peak avalanches, mount rainier, washington. *Journal of Volcanology and Geothermal Research*, 139(1):89 – 102. Modeling and Simulation of Geophysical Mass Flows.

Sheridan, M. F. and Macas, J. (1995). Estimation of risk probability for gravity-driven pyroclastic flows at volcan colima, mexico. *Journal of Volcanology and Geothermal Research*, 66(1):251 – 256. Models of Magnetic Processes and Volcanic Eruptions.

Sheridan, M. F., Patra, A. K., Dalbey, K., and Hubbard, B.

Silbert, L. E., Ertas, D., Grest, G. S., Halsey, T. C., Levine, D., and Plimpton, S. J. (2001). Granular flow down an inclined plane: Bagnold scaling and rheology. *Physical Review E*, 64(5):051302.

Spiller, E. T., Bayarri, M. J., Berger, J. O., Calder, E. S., Patra, A. K., Pitman, E. B., and Wolpert, R. L. (2014). Automating emulator construction for geophysical hazard maps. *SIAM/ASA Journal on Uncertainty Quantification*, 2(1):126–152.

Stefanescu, E. R., Bursik, M., Cordoba, G., Dalbey, K., Jones, M. D., Patra, A. K., Pieri, D. C., Pitman, E. B., and Sheridan, M. F. (2012a). Digital elevation model uncertainty and hazard analysis using a geophysical flow model. *Proceedings of the Royal Society of London A: Mathematical, Physical and Engineering Sciences*, 468(2142):1543–1563.

Stefanescu, E. R., Bursik, M., and Patra, A. K. (2012b). Effect of digital elevation model on mohr-coulomb geophysical flow model output. *Natural Hazards*, 62(2):635–656.

Stein, M. (1987). Large sample properties of simulations using latin hypercube sampling. *Technometrics*, 29(2):143–151.

Sulpizio, R., Capra, L., Sarocchi, D., Saucedo, R., Gavilanes-Ruiz, J., and Varley, N. (2010). Predicting the block-and-ash flow inundation areas at volcán de colima (colima, mexico) based on the present day (february 2010) status. *Journal of Volcanology and Geothermal Research*, 193(1):49 – 66.

Tang, B. (1993). Orthogonal array-based latin hypercubes. *Journal of the American Statistical Association*, 88(424):1392–1397.

Voellmy, A. (1955). Über die Zerstörungskraft von Lawinen. *Schweiz Bauzeitung*, 73:159–165, 212–217, 246–249, 280–285.

Webb, A. (2004). Granular flow experiments to validate numerical flow model, TITAN2D. Master's thesis, University at Buffalo.

Webb, A. and Bursik, M. (2016). Granular flow experiments for validation of numerical flow models. Technical report, University at Buffalo.

Wieland, J. M., Gray, J. M. N. T., and Hutter, K. (1999). Channelized free-surface flow of cohesionless granular avalanches in a chute with shallow lateral curvature. *Journal of Fluid Mechanics*, 392:73–100.

Yu, B., Dalbey, K., Webb, A., Bursik, M., Patra, A. K., Pitman, E. B., and Nichita, C. (2009). Numerical issues in computing inundation areas over natural terrains using Savage-Hutter theory. *Natural Hazards*, 50(2):249–267.

Zobin, V., Luhr, J., Taran, Y., Bretón, M., Cortés, A., Cruz-Reyna, S. D. L., Domínguez, T., Galindo, I., Gavilanes, J., Muniz, J., Navarro, C., Ramírez, J., Reyes, G., Ursúa, M., Velasco, J., Alatorre, E., and Santiago, H. (2002). Overview of the 1997–2000 activity of volcán de colima, méxico. *Journal of Volcanology and Geothermal Research*, 117(1):1 – 19.

Zobin, V. M., Arámbula, R., Bretón, M., Reyes, G., Plascencia, I., Navarro, C., Téllez, A., Campos, A., González, M., León, Z., Martínez, A., and Ramírez, C. (2015). Dynamics of the january 2013–june 2014 explosive-effusive episode in the eruption of volcán de colima, méxico: insights from seismic and video monitoring. *Bulletin of Volcanology*, 77(4):31.